Manuscript prepared for Atmos. Meas. Tech. Discuss.
with version 2014/07/29 7.12 Copernicus papers of the LaTeX class copernicus.cls.
Date: 24 December 2015

Design and characterization of specMACS, a multipurpose hyperspectral cloud and sky imager

F. Ewald[1,*], T. Kölling[1,*], A. Baumgartner[2], T. Zinner[1], and B. Mayer[1]

[1]Ludwig Maximilians Universität, Institut für Meteorologie, Munich, Germany
[2]Deutsches Zentrum für Luft und Raumfahrt, Institut für Methodik der Fernerkundung, Oberpfaffenhofen, Germany
[*]These authors contributed equally to this work.

Correspondence to: T. Zinner (tobias.zinner@lmu.de)

Abstract

The new spectrometer of the Munich Aerosol Cloud Scanner (specMACS) is a multipurpose hyperspectral cloud and sky imager designated, but not limited to investigations of cloud-aerosol interactions in Earth's atmosphere. ~~Equipped with a~~ With its high spectral and spatial resolution, the instrument is designed to measure solar radiation in the visible and short-wave infrared region that is reflected from, or transmitted through clouds and aerosol layers. It is based on two hyperspectral ~~line~~ cameras that measure in the solar spectral range between 400–2500 nm with a spectral bandwidth between 2.5–12.0 nm. The instrument was already operated in ground-based campaigns as well as aboard the German High Altitude LOng Range (HALO) research aircraft, e.g. during the ACRIDICON-CHUVA campaign in Brazil during summer 2014.

This paper describes the specMACS instrument hardware and software design and characterizes the instrument performance. During the laboratory characterization of the instrument the radiometric response as well as the spatial and spectral ~~performance~~ resolution was assessed. Since the instrument is primarily intended for retrievals of atmospheric quantities by inversion of radiative models using measured radiances, a focus is placed on the determination of its radiometric response. Radiometric characterization was possible for both spectrometers with an absolute accuracy of 3 % at their respective central wavelength regions. First measurements are presented which demonstrate the application possibilities and show that the key demands on radiometric and spectral accuracy as posed by the intended remote sensing techniques are fulfilled.

1 Introduction

The spectrally resolved measurement of solar radiation is a long standing method in earth science. In the beginning half of the 20th century Gordon Dobson introduced the method of spectroscopy into the field of atmospheric remote sensing. On the basis of passive measurements of the absorption of solar radiation by stratospheric ozone he deter-

mined the depth and variability of the ozone layer. Since then the exploitation of atmospheric ~~absorption to measure the concentration of atmospheric constituents~~ and particle absorption has led to the development of spaceborne measurement platforms like the ~~Infrared Atmospheric Sounding Interferometer (IASI) and the Cross-track Infrared Sounder (CrIS~~Moderate-resolution Imaging Spectroradiometer (MODIS) or the Earth Observing-1 Mission (EO-1) for spectral remote sensing of ~~temperature and~~ trace gas profiles and cloud properties.

Remote sensing of cloud and aerosol parameters is still mostly done by use of multi-spectral sensors, i.e., using only a limited number of spectral bands. Prominent examples are, e.g., ground-based aerosol retrievals using CIMEL sun-photometers in the Atmospheric Radiation Measurement Program and the Aerosol Robotic Network (AERONET) (Holben et al., 1998) or satellite based multi-channel techniques following ~~, e.g.,~~ Hansen and Pollack (1970); Twomey and Cocks (1989) and Nakajima and King (1990) for remote sensing of cloud properties. However, the application of spectrally resolved, hyperspectral techniques in cloud and aerosol remote sensing is still in its early stages.

Systems like the Solar Spectral Flux Radiometer (SSFR, Pilewskie et al., 2003) or the Spectral Modular Airborne Radiation measurement sysTem (SMART, Wendisch et al., 2001; Wendisch and Mayer, 2003) were used for cloud remote sensing from ground (McBride et al., 2011; Chiu et al., 2012; Jäkel et al., 2013) or airborne perspective ~~e.g. Ehrlich et al. (2008); Eichler et al. (2009); Schmidt et al. (2007)~~ (Ehrlich et al., 2008; Eichler et al. Coddington et al. (2010). While most techniques from these two instruments still use only a few channels to derive cloud optical thickness or cloud particle size from solar transmissivity or reflectivity measurements (Kikuchi et al., 2006; Coddington et al., 2010; McBride et al., 2011) some first techniques use spectral slopes for identification of cloud phase (Ehrlich et al., 2009; Jäkel et al., 2013). Only recently Coddington et al. (2012) and LeBlanc et al. (2015) proposed and systematically tested a range of characteristics of the full spectrum to be used for general ground-based cloud remote sensing. All of these methods are based on non-imaging sensors, i.e., only one measurement is taken at a time and one line of

measurements is constructed by sensor motion or cloud motion over a ground-based measurement.

There already exist some imaging spectroscopy instruments for the ground-based or airborne remote sensing perspective. In the visible wavelength range, one of the earliest instruments was the Compact Airborne Spectrographic Imager (CASI, Babey and Anger (1989)) with 288 spectral channels (2.5 nm resolution). Over the years, CASI measurements were used in various applications in atmospheric sciences. Naming only a few, Wendling et. al. (2002) investigated aerosol-radiance interactions, Mayer et al. (2004) determined water cloud droplet size distributions using the backscatter glory and Zinner and Mayer (2006) assessed retrieval biases due to inhomogeneity of stratocumulus clouds. Further cloud remote sensing applications were done with the AisaEAGLE instrument from SPECIM, which covers the spectral range between 400–970 nm with a spectral resolution of 2.9 nm. From the ground-based perspective, Schäfer et al. (2013) retrieved cirrus optical thickness and ice crystal shape, while Bierwirth et al. (2013) and Schäfer et al. (2013) used the instrument to retrieve optical thickness and effective radius of Arctic boundary-layer clouds from the airborne nadir perspective. The Airborne Visible/InfraRed Imaging Spectrometer (AVIRIS, Green et. al. (1998)) extended the measurement range into the near-infrared spectrum with 224 spectral channels (10 nm resolution) between 400–2500 nm. Gao et. al. (1993) already used it to detect cirrus clouds using the information in the near-infrared, while Thompson et. al. (2015) used the higher spectral resolution (5 nm) with 600 spectral channels of AVIRIS-NG for the remote detection of methane. A further imaging spectroscopy instrument is the Airborne Prism EXperiment (APEX) imaging spectrometer (Itten et al., 2008; Schaepman et al., 2015) with 532 spectral channels and a spectral resolution between 0.9–12.3 nm. Exploiting this high spectral resolution, Popp et al. (2012) used APEX for high-resolution remote sensing of NO2. With 1056 spectral channels in the 400–2500 nm spectral region, the specMACS instrument continues the development of atmospheric radiation measurements towards imaging spectroscopy.

As commercially available spectral imagers for measurements in the solar visible and near-infrared spectrum become more and more affordable they become more frequently used nowadays. For airborne remote sensing of land surfaces a few, still costly commercial solutions are available at the moment. Based on spectral off-the-shelf camera systems, ~~very similar to core sensors used in these solutions,~~ the Meteorological Institute of the University of Munich decided to tailor a system to its specific needs. In the following this new hyperspectral imaging instrument for atmospheric measurements on ground-based and airborne platforms with a spectral coverage of 400–2500 nm will be introduced and characterized in detail. On the basis of some first applications the scientific data obtained with the specMACS instrument will be introduced.

1.1 Conceptual embedding

The institute already hosts a range of instruments for remote measurements of the atmosphere: an aerosol lidar, a millimeter-wave cloud radar, a sun-photometer and multiple Differential Optical Absorption Spectroscopy (DOAS) instruments. Using this active and passive instrumentation, improvements of our understanding of the aerosol-cloud interaction in the atmosphere ~~is~~ are pursued. Cloud microphysical development like droplet growth, glaciation processes, ice nucleation as well as cloud dynamics are influenced by the abundance and type of available cloud nuclei, the fraction of the aerosol background which can act as nucleus for droplet or ice particle growth. These microphysical processes are of greatest interest for the understanding of future climate development (Houghton et al., 2001).

To this end Marshak et al. (2006a); Martins et al. (2011); Zinner et al. (2008) and Ewald et al. (2013) proposed cloud side scanning measurements to observe the basically vertical development of cloud particles. To retrieve particle size and thermodynamic phase they propose to use reflected solar radiation in the near-visible to near-infrared spectral regions. This application is a core goal for the development of the new sensor. With the help of an imaging spectrometer the required spatially resolved measurements ~~becomes~~ become possible. Especially the vertical dimension of these observations should reflect many as-

pects of cloud-aerosol-interaction as well as mixing of cloudy and ambient air (Martins et al., 2011; Rosenfeld et al., 2012). For the same partially cloudy scenes, additional remote measurements of interacting aerosol characteristics (particle type, size, amount) as well as of some gaseous atmospheric components will become accessible by exploitation of the spectral image information.

1.2 Accuracy considerations

The complexity of cloud geometry and three-dimensional radiative effects related to it pose a great challenge to cloud side remote sensing. Various studies of Varnai and Marshak (2002); Marshak et al. (2006b) and Zinner and Mayer (2006) quantified the impact of three-dimensional radiative effects on particle size retrievals based on 1D radiation transfer simulations like Nakajima and King (1990) and found an overestimation of effective radius by up to $2\,\mu m$ (Cornet et al., 2005) with a standard deviation of $1.5\,\mu m$ (Bréon and Doutriaux-Boucher, 2005). Especially for spatially high resolved cloud side measurements ($< 100\,m$) standard deviations to the true effective radius can be 20 % and more (Zinner and Mayer, 2006).

The proposed retrieval method by Martins et al. (2011) and Zinner et al. (2008) tries to account for this uncertainty by means of a statistical retrieval based on fully 3-D radiative transfer simulations. For optically thick liquid water clouds an uncertainty in effective radius of $2\,\mu m$ relates roughly to a radiance uncertainty of 20 % at the near-infrared wavelength $2100\,nm$ used in the retrieval of (Nakajima and King, 1990). To limit the uncertainty in microphysical retrievals due to sensor characteristics~~well below this uncertainty caused by 3-D radiative effects~~, we aim for an absolute radiometric calibration uncertainty ~~of 5or below . A systematic deviation of about 10in radiance would, in most cases, produce an additional error for the retrieved quantities which would reach uncertaintyvalues associated with mentioned 3-D effects~~well below the retrieval uncertainty.

Spectral accuracy requirements are not too strict for current microphysical cloud retrievals, as no sharp absorption line is evaluated. ~~In order to exploit the different absorptions of smaller and larger cloud particles in the near infrared an spectral bandwidth and accuracy~~

of 10–50is supposed to be sufficient. NeverthelessHowever, the solar spectrum itself exhibits many narrow absorption lines. For this reason, the spectral accuracy should be comparable or better than the spectral bandwith of the instrument. The radiometric accuracy can be compromised if resolved absorption lines are spectrally misaligned. Furthermore, measurements of accurate and highly resolved spectra are invaluable for the application of novel retrieval techniques since various spectral atmospheric and soil features become exploitable. Spectrally high resolved measurement is needed High spectral resolution measurements are needed in the VNIR spectral range where many narrow absorption features are located, e.g., for photon path analysis using the optical depth of the oxygen A-band or for the detection of surface albedo influence on the basis of known spectral vegetation features. Conceivable use of the spectral data to estimate the oxygen A-band depth tightens spectral accuracy requirements to a few nanometer or less (Fischer and Grassl, 1991). As shown by Heidinger and Stephens (2000) , the retrieval of the total column optical depth of the oxygen A-band is limited by the spectral resolution of the instrument.

This work is based on previous work which developed hyperspectral instruments and their calibration. The general principle of measurement and the specific implementation of the used hyperspectral instrument was developed and described in detail by Aikio (2001). Jørgensen (2002) examined this design and described necessary steps in its calibration, potential error sources and their mitigation. The overall approach to the calibration is based on the work of Lenhard et al. (2015) and was carried out in close cooperation with the Remote Sensing Technology Institute (IMF) of the German Aerospace Center (DLR).

This paper is organized as follows: Sect. 2 first introduces the new specMACS instrument and its measurement principle. Next, all necessary technical amendments and software developments are introduced that make specMACS a versatile and accurate cloud remote sensing instrument usable for airborne push-broom applications as well as for ground-based cloud side or hemispheric scan(Sect. **??**). In Sect. 3 the methods used during characterization and calibration of the instrument are introduced and described. Following each subsection, detailed results of the radiometric and spectral sensor characterisation are given and discussed. Finally application examples are shown, presenting the first air-

borne deployment of the instrument on-board HALO, the German high-altitude long range research aircraft (Sect. 4). Cloud side measurements were collected through a customized side window of the aircraft during the Brazilian-German ACRIDICON-CHUVA campaign in autumn 2014.

2 The specMACS instrument

The spectrometer of the Munich Aerosol Cloud Scanner (specMACS) is an imaging spectrometer system for the measurement of solar radiation in the 400–2500 nm wavelength range, which is based on two hyperspectral ~~line~~ cameras. It is designed for remote sensing of cloud and aerosol optical properties and atmospheric trace gases. The emphasis is on the development of new ground-based retrieval methods of clouds as well as on the understanding of 3-D radiative effects in already existing retrieval methods. Key properties of the two imaging spectrometers that were determined in this work are given in Table 1. The instrument was developed at the Meteorological Institute of the Ludwig Maximilians University and is usually operated on the roof platform of the institute. ~~A scanning setup allows to capture a two dimensional image with spectral information on every spatial pixel. This is illustrated in Fig. **??** by an exemplary hyperspectral data cube as measured with specMACSon the research aircraft HALO. While the hyperspectral line was arranged perpendicular to the scan path (across track) the scanner was used to create an image of cloud sides along track of the scan path. During this push-broom-like scan an highly resolved spectrum of reflected solar radiation was measured as shown in Fig. **??** where prominent absorption lines in this wavelength region are indicated. In the following the terms *along track* and *across track* denote directions perpendicular and parallel to the spatial line respectively.~~

2.1 Instrument concept

The instrument comprises two commercially available hyperspectral line spectrometers built by SPECIM (Specim Spectral Imaging Ltd., Oulu, Finland.). Combined, these hyperspectral

cameras simultaneously acquire light spectra between 400–2500 nm for one spatial dimension. The measurement principle is based on the diffraction of a ~~beam of light perpendicular to the entrance slit of the sensor as shown in Fig. 2. Both spectrometers are equipped with front optics, a transmission grating and a CMOS camera. After the light has passed through the front optics L_1 a slit beam is shaped by a narrow ($\approx 30\,\mu m$) entrance slit in the image plane. This beam contains light from~~ light beam by a Volume Phase Holographic (VPH) Transmission Grating after one spatial dimension ~~as the second spatial dimension is masked out by the slit . Before the light beam gets diffracted it is collimated by optics L_2 in front of the spectrograph. The beam is then passed through a Prism-Grating-Prism (PGP) spectrograph, which is composed of a transmission grating embedded between two prisms (P_1 and P_2). This Volume Phase Holographic (VPH) Transmission Grating is made of bichromated gelatin which contains periodical changes in the refractive index.Following Bragg's law (Bragg and Bragg, 1913) ,~~

$$m\lambda = d(\sin\alpha + \sin\beta) = 2d\sin\theta_B\,,$$

~~monochromatic light with wavelength λ entering the grating under angle α gets diffracted under the specific angle β. Here m is an integer and denotes the specific diffraction order while d is the gratingspacing. The diffraction for wavelength λ_B is maximized when the angle of diffraction β equals the angle of incidence α, which is known as the Bragg condition. For this reason the first prism P_2 refracts the light beam at the Bragg angle θ_B onto the grating after the beam is collimated by the entrance optics of the spectrograph.~~

~~A second prism P_2 refracts the light from the $m = -1$ Bragg diffraction order back again in such a way that the light with one (central) wavelength λ_c aligns with the optical axis of the system. Nearby wavelengths get spread along the axis perpendicular to the spatial dimension of the light beam. This setup facilitates the spectral diffraction of the beam along the optical axis, which simplifies the instrument design and reduces the overall instrument size. Behind the PGP-element the beam is then focused on a second image plane by the focusing lens L_3. In this plane~~ has been filtered by an entrance slit ($\approx 30\,\mu m$

for both spectrometers) as shown in Fig. 2. After the grating, the spatial variations of the radiant flux are captured on one dimension of an CMOS active pixel sensor (APS) (Fossum, 1997) ~~then measures the radiant flux of the spectrally separated beam. While the spatial variations of the radiant flux are captured on one dimension its~~ while the spectral variations are registered on the other dimension~~of the sensor~~. An order blocking filter (OBF) is mounted just in front of the APS to prevent spectral overlap of different diffraction orders~~m~~. A detailed description of the measurement principle and the specific implementation of the used hyperspectral instrument can be found in Aikio (2001) .

2.2 VNIR spectrometer

The spectral camera PFD (SPECIM SP-PFD-CL-65-V10E) is used for the coverage of the visible and near-infrared wavelength range (400–1000 nm) (which in the following is referred to as the visible near-infrared, VNIR). It is equipped with a 18.5 mm $f/2.4$ front lens (OLE18.5). Inside the spectrograph (ImSpector V10E) the entrance slit, the collimating optics, the PGP-element and the focusing optics are firmly connected together. Its linear dispersion is specified with 97.5 nm mm^{-1}. In front of the sensor region corresponding to longer wavelengths originating from first order $m = -1$ diffraction an order blocking filter (SPECIM OBF 570) is placed to prevent light of shorter wavelengths from second order $m = -2$ diffraction to reach the sensor. The sensor is based on a camera (MV1-D1312-160) from Photonfocus, which is built around the monochrome, uncooled CMOS active pixel sensor (A1312) from Photonfocus. This sensor is backside-illuminated to increase its low-light performance. ~~The most important parameters are listed~~ It provides a resolution of 1312 $\times$ 800 pixels with a pixel distance on chip (pixel pitch) of 8 µm $\times$ 8 µm and an active optical area of 10.48 mm $\times$ 8.64 mm. The field of view (FOV) along the spatial line is 32.7°, while the instantaneous field of view (IFOV) for a single pixel is 1.37 mrad across and 2.00 mrad along the spatial line. The entrance slit width of 30 µm limits the average spectral resolution to 3.1 nm with an average spectral sampling of 0.8 nm. Due to noise, the useable dynamic range for a single frame of the VNIR camera is approximately 9.5 bit. Further parameters can be found in Table 1.

2.3 SWIR spectrometer

For the wavelength region between 1000–2500 nm the SWIR spectrometer (SPECIM SP-SWIR-LVDS-100-N25E) is used (which in the following is referred to as the shortwave infrared, SWIR). It is equipped with a 15 mm $f/2.1$ front optic lens (OLES15). Since the solar radiance decreases strongly from 1000 to 2500 nm the usable dynamic range over the complete wavelength range would be very limited. A spectral flattening filter (Hebo RC 01, SPECIM) is therefore placed in front of the lens to attenuate the shorter wavelengths and thereby improve the overall use of the dynamic range of the sensor for solar radiation. This filter has an additional special coating to block the wavelength range from 800–960 nm since the SWIR sensor is already sensitive from 800 nm onwards and since these wavelengths cannot be filtered by an order blocking filter. The linear dispersion of its spectrograph (ImSpector N25E) is specified with 208 nm mm^{-1}. ~~Just like in the case of the VNIR~~Similar to the VNIR, an order blocking filter (OBF 1400) is placed in front of the SWIR sensor to prevent spectral overlap from different diffraction orders. The SWIR spectrometer uses the MARS SW 320 $\times$ 256 sensor from SOFRADIR with a pixel pitch of 30 µm. The HgCdTe-based detector is thermoelectrically cooled to 200 K to reduce the level of dark current noise. The ~~most important~~ FOV along the spatial line is 35.5° while the IFOV is 3.79 mrad across the spatial line and 1.82 mrad along the spatial line. The entrance slit width of 30 µm limits the average spectral resolution to 10.3 nm with an average spectral sampling of 6.8 nm. Due to the strongly varying dark signal, the noise-limited usable dynamic range for a single frame of the SWIR camera varies in the range of 11–11.6 bit, depending on integration time and environment conditions. More detailed information is given in 3.1.1. Further parameters are listed in Table 1

2.4 Stray light protection

~~During zenith cloud measurements obvious signs of stray lightwere observed. This became clear when the front optics were temporarily shielded from light from outside the field of~~

view, which resulted in a significant drop in measured radiance. In particular, direct solar radiation onto the unshielded front optics affected the radiometric accuracy while the stray light was hard to detect in scenes with low temporal variabilityBoth, the VNIR and the SWIR sensor are affected by stray light, however the effects on the SWIR sensor are typically a few times stronger than on the VNIR. In Fig. 3, the effect of stray light and its mitigation is exemplarily shown using a prototype of the actual stray light protector. To mitigate the effects of stray light permanently, a system of shielding baffles which are placed in front of the cameras optics (Fig. 4) was designed. The stray light protector was built of aluminium which was sandblasted, anodized and painted with NEXTEL Velvet Black paint. According to Dury et al. (2007), the regular and diffuse single scattering reflectance of this coating is typically less than 5 % in the whole spectral range of both spectrometers. Simulations showed that these baffles attenuate incident light that originates from angles more than 15 ° outside the FOV by at least 2–3 orders of magnitude. After implementing the stray light protection, no visible evidence of stray light was found during ground measurements with the sun outside the FOV by more than 15 °.

2.5 Scanning mountInstrument automation

For ground based measurements, specMACSis mounted on a scanning mount (MESU-OPTICS Mesu-Mount 200) with two rotating axes (vertical and horizontal). This allows the instrument to be pointed anywhere in the upper hemisphere and to perform precise and repeatable automated scans. The scanning mount is equipped with a customized closed loop motor controller (based on a ROBOTEQ Inc., SDC2130). It is equipped with an optical relative position encoder, which allows to control the full turn of each axis in 10000 steps resulting in a relative positioning accuracy of the angle of about two steps, which is accordingly 0.072° and thereby in the same order as the sensors IFOV (Instantaneous Field Of View). The closed loop control allows to record the actual position of the cameras reliably even if the motors are slipping, stuck or moved by hand. The scanning mount can be controlled using the newly developed acquisition control system as outlined

below and includes manual control via a wireless controller and automated control using the CAMPaign ASistant (CAMPAS) software introduced in the following section.

3 Software

The specMACS hyperspectral imager is a multipurpose measurement system, which produces data at a rate of up to $300\,\mathrm{MiB\,s^{-1}}$ and which must be stored reliably on disk, even when operated continuously for hours. An important goal of the system design is further to provide a very flexible base system which can be reconfigured to various differing measurement campaign scenarios (e.g. ground based on a scanner vs. airborne use as push-broom instrument) and augmented with additional sensor information (e.g. scanning mount, temperature or position). All of this should be possible without rewriting the entire software and without the need of complex manual intervention when clouds are passing by and time is scarce. Especially for an airborne setup with limited operator availability, the system must be able to run fully autonomouseven in the case of unexpected errors. These constraints led to the modular and distributed software concept as described below.

2.1 Software concept

To provide a measurement system which can be adapted to the various measurement purposes we designed a flexible and open software system design that can be adapted to various measurement scenarios easily. Although we opted for a highly modular and distributed software concept, we still had to ensure that the system is capable of maintaining the constantly high data load as presented by the hyperspectral imagers. We decided to use ZeroMQ (Hintjens, 2010) as communication middleware, which was evaluated by CERN (Dworak et al., 2011, 2012) intensively.

The system is inspired by the actor model (Hewitt et al., 1973) and Erlang/OTP (Armstrong, 2007) . For each individual task we use an independent actor (which can also

be thought of as a server). Every actor communicates via various ZeroMQ sockets with other actors and is constantly monitored by a supervisor. Each actor can be written in any programming language and can be started or stopped at any time, independently of all other actors. As this design limits failures to short term interruptions of small parts of the system, it greatly improves resilience compared to previous monolithic implementations. autonomous.

The main data flow can be seen in Fig. **??**. Each camera has an associated grabber which receives the captured data stream. All captured data is immediately stored to disk while a reduced data stream is simultaneously extracted by several live processing units. This reduced data stream is sent to the user interface and an automated exposure control system. Without interfering with the original data stream the automated hardware control system is able to analyze and act upon incoming signals or user inputs.

2.1 Instrument automation

During ground-based scans or unsupervised airborne operation the integration time t_{int} has to be be adjusted to avoid over- as well as underexposure. For this reason a control software was developed for the specMACSsystem which automatically sets integration time and controls Furthermore, frequent dark frame measurements . Since are necessary since the dark current signal of the SWIR sensor varies strongly with integration time and ambient air temperaturefrequent dark frame measurements are necessary.

2.0.1 Auto exposure

The main task of the auto exposure control system, setting the integration time t_{int} to an optimized value, was designed with three goals of descending importance in mind: Since clouds as the main object of interest are typically the brightest parts of a scene, overexposure is to be avoided in any case. To limit the number of distinct dark current

measurementsand to facilitate later data analysis, only a few discrete integration times will be used. These are indicated as $t_{\mathrm{int}}(i)$ in the following. However, to recover from very bright scenes and to use the available dynamic range of the sensor in an optimal way, integration time should be increased after a certain time span of underexposed conditions.

In Fig. 25 the overall logic of the integration time regulation of the auto exposure software is illustrated. The logic is based on a histogram of the signal which is evaluated in real-time over all CMOS pixels. From the histogram, the 99th percentile (q_{99}) is calculated and stored for subsequent analysis. The q_{99} was chosen since it turned out to be a more stable indicator for current signal levels than the maximum value, which is sensitive to signal noise and bad pixels.

A limited set of integration times $t_{\mathrm{int}}(i)$ were used during the aircraft measurement campaign ACRIDICON 2014: 0.5, 0.85, 1, 1.2, 1.5, 2, 3, 5, 8, 12. For this reasons, a control software automatically sets integration time and controls dark frame measurements, 18 and 25ms. These values were chosen as a compromise between a sufficient range of values, reasonably small steps (less then a factor of 2) between integration times and the goal to have only a limited amount of distinct integration times.

The following algorithm is in principle independent of the frame rate, but was tested and optimized for 30 fps. To avoid overexposure, the 99th percentile q_{99} of the signal histogram is limited to $3/4$ of the full dynamic range of the sensor in order to provide headroom for transient radiance peaks. If this limit is exceeded for more than four frames within the last 150 frames, the integration time $t_{\mathrm{int}}(i)$ is reduced to the next allowed value $t_{\mathrm{int}}(i-1)$. After such an overexposure protection is triggered, no increments to longer integration times are allowed during the following 1800 frames.

To recover from a reduced integration time, the auto exposure control periodically tries to increase the integration time t_{int}. To this end, the histograms of the last 150 frames are

periodically extrapolated to the next longer integration time $t_{\mathrm{int}}(i+1)$. If the extrapolated histograms do not trigger the overexposure protection described above, $t_{\mathrm{int}}(i)$ is increased to $t_{\mathrm{int}}(i+1)$. Thereby any increase of integration time is tested before it is actually performed and suppressed if the signal limit set by the quantile limit would be exceeded.

2.0.1 Automatic dark frame

Another task of the control software is the automation of dark signal measurements. During dark signal measurements, it is obviously not possible to perform real measurements, so the amount of time spent with dark signal measurements is to be minimized. However, the dark signal varies with time, so the automation is set up to measure approximately 30 dark frames at least every two minutes. Since the dark signal additionally changes with integration time $t_{\mathrm{int}}(i)$, the system checks if a recent dark signal measurement with the current sensor settings was obtained and if not, triggers a dark signal measurement before changing $t_{\mathrm{int}}(i)$pontentionally resulting in additional (non-instantaneous) 5.6 bit of dynamic range for each sensor. Details of the automated control software are described in detail in appendix A.

2.0.1 Scriptable measurements

In order to control and repeat complex measurement tasks, the CAMPaign ASsistant (CAMPAS) was developed. It is a domain specific scripting language combined with a communication library which has access to all system components. Using CAMPAS the user can define measurement tasks like a hemispherical scan through step-by-step instructions These instructions control the behavior of the sensors, the scanning mount and all other system components combined. The CAMPAS system furthermore provides simple access to various dynamic coordinates (e.g. sun position or the current position of other instruments). Thus a general task can be written once and repeated many times, which increases comparability of results.

3 Characterization and calibration methods

There are three essential characteristics which define the overall performance of imaging spectrometers. First, the radiometric response of the instrument has to be known to obtain absolute radiometric measurements. Secondly, a precise knowledge about the spectral projection onto the sensor is required to put the radiometric values into context. Concluding, information about the spatial projection and its geometric distortions are required to asses the spatial image quality and its resolution. Additional to the mostly stable sensor characteristics, faster varying data, like the sensors settings, orientation and dark signal need to be captured during measurement. Armed with this information measured raw data can be converted into physical units during the calibration procedure. ~~Additional to the measured raw data, several auxiliary datasets are needed for the calibration procedure. This auxiliary data includes dark current measurements made before and after each measurement as well as the instrument characteristics obtained during a laboratory characterization.~~

A guideline through the whole process and the involved quantities is given by the calibration flow chart in Fig. 5. The process follows Lenhard et al. (2015) closely and is extended by a nonlinearity correction regarding integration time explained in Sect. 3.1.2. The following subsections will cover each of the displayed steps.

In the following all variables are given as pixel-wise properties when not mentioned otherwise. Temporal averaged properties of the sensor will be identified with angle brackets while spatial averages will be indicated with an overbar. The laboratory characterization of the specMACS sensors was performed at the Calibration Home Base (CHB) (Gege et al., 2009) of the Remote Sensing Technology Institute ~~(IMF)~~ of the German Aerospace Center~~(DLR)~~.

3.1 Radiometric characterization

The sensors consist of many mostly independent pixels of which each acts as a radiance sensor for its specific spectral and spatial section of the full image. ~~Each pixel outputs the measured signal as a digital number. To obtain an absolute radiometric value the sensor~~

has to be calibrated since its signal is subject to influences other than the impinging light. The sensor signal S can be modeled as a sum of a radiometric signal S_0 containing only radiance information, S_d which describes the dark signal of the sensor and the noise $\mathcal{N}$ of the sensor:

$$S = S_0 + S_\mathrm{d} + \mathcal{N}$$

In the following subsections noise $\mathcal{N}$, dark signal S_d and radiometric signal S_0 will be independently examined. In the remaining subsections bad pixels and optical performance like angular and spectral bandwidth as well as keystone effects will be discussed.

3.1.1 Noise

The noise $\mathcal{N}$ is composed of dark current noise $\mathcal{N}_\mathrm{dc}$, read noise $\mathcal{N}_\mathrm{read}$ and photon shot noise $\mathcal{N}_\mathrm{shot}$. Their joint standard deviation $\sigma_\mathcal{N}$ is calculated using the individual standard deviations σ_shot, σ_dc and σ_read:

$$\sigma_\mathcal{N} = \sqrt{\sigma_\mathrm{shot}^2 + \sigma_\mathrm{dc}^2 + \sigma_\mathrm{read}^2} = \sqrt{k^2 N + \sigma_\mathrm{dark}^2}.$$

Since photons arrive randomly in time the number N of photoelectrons measured during a fixed time interval is distributed according to the Poisson distribution. Following the Poisson statistics the standard deviation σ_N of a distribution with the expectation value N is proportional to $\sqrt{N}$. For this reason the photon shot variance σ_shot^2 scales linearly with the number of incoming photoelectrons N and the squared conversion gain k^2 [DN^2] (Eq. 12). For a sensor with linear response, the relation $S_0 \propto N$ holds. A deviation from this relationship can be an indication for a nonlinear relationship between the number N of photoelectrons and the photoelectric signal S_0 or is caused by a non-Poisson noise source.

Similar to the dark signal S_d in S, a dark noise $\mathcal{N}_\mathrm{dark}$ remains in $\mathcal{N}$ without illumination. It is comprised of dark current noise $\mathcal{N}_\mathrm{dc}$ and readout noise $\mathcal{N}_\mathrm{read}$. The dark current noise is caused by statistical variation of thermally generated electrons. Like the photon noise its origin is a random process and therefore exhibits a Poisson distribution. Pixel readout and analog to digital conversion is further subject to electronic readout noise, which is independent from integration time.

With the classic Photon Transfer Curve (PTC) (Janesick, 2007) the noise characteristics can be used to determine many important camera parameters. When the signal noise standard deviation $\sigma_\mathcal{N}$ is plotted against the mean, darkcurrent-corrected signal level $\langle S_0 \rangle$ on a log-log scale different noise regimes become apparent. The dark noise at integration time $t_\mathrm{int} = 0\,\mathrm{s}$ at the lower end of $\langle S_0 \rangle$ is dominated by read-out noise with standard deviation σ_read. With increasing mean signal level $\langle S_0 \rangle$ photon shot noise becomes dominant with σ_shot. Due to the Poisson-like distribution the photon shot noise variance σ^2_shot should scale linearly with mean signal level. Deviations from this linear relationship can provide an indication of a nonlinear radiometric response (Bohndiek et al., 2008) or a charge sharing mechanism between pixels (Downing et al., 2006; Stefanov, 2014) .

Since both sensors can not be homogeneously illuminated (as required in classic PTC) due to the spectrographic diffraction grating, the noise standard deviation $\sigma_\mathcal{N}$ and mean, darkcurrent-corrected signal level $\langle S_0 \rangle$ are calculated individually for each pixel. For this analysis $\sigma_\mathcal{N}$ is calculated as the pixel-wise standard deviation of 500 consecutive frames measured on an integrating sphere for multiple integration times t_int. As noise $\mathcal{N}$ describes unbiased temporal variations of the signal around its expectation value, its temporal mean vanishes: $\langle \mathcal{N} \rangle \approx 0$.

In addition to noiseThereby, pixel sensors are also subject to inter-pixel variations caused by imperfections in the sensor material and electronics. These variations are almost constant in time but become evident on uncorrected images as visible noise pattern. This pat-

tern is generally called fixed pattern noise (FPN) and can be mitigated through calibration using characterized parameters ~~from~~ determiend in the following sections. Long term variations of the FPN can be covered through periodic recharacterization of the sensor.

~~Figure 13 shows the results of the noise analysis which was obtained from the nonlinearity measurements with varying integration times as listed in Table 2. For each pixel and each integration time, the mean and standard deviation was calculated and accumulated in the shown 2-D histograms. The noise characteristics of the VNIR are shown on the left while results for the SWIR are shown on the right. On top in Fig. 13 the pixel-wise standard deviation $\sigma_\mathcal{N}$ is plotted against the mean, darkcurrent-corrected signal level $\langle S_0 \rangle$ on a log-log scale. On the bottom, the same is done with the pixel-wise variance $\sigma^2_\mathcal{N}$ on a linear scale.~~

~~At low values of $\langle S_0 \rangle$ the signal-independent read-out noise becomes apparent. The read-out noise for $t_{\text{int}} = 0\,\text{s}$ is derived as the y-intercept of a constant fit on $\sigma_\mathcal{N}$ for $\langle S_0 \rangle < 30\,\text{DN}$. By doing this, the noise associated with the readout channel was found to be 5.0 DN for the VNIR and 4.5 DN for the SWIR spectrometer. For larger values of $\langle S_0 \rangle$ the noise begins to increase.~~

~~When the standard deviation $\sigma_\mathcal{N}$ is fitted with the square root model following Eq. (12)the noise characteristics can be further investigated. At first glance, the noise standard deviation of the VNIR sensor is in accordance with the noise model described by Eq. (12) with a constant conversion gain $k = 0.043\,\text{[DN]}$. For values of~~ Each pixel outputs the measured signal as a digital number (DN). To obtain an absolute radiometric value the sensor has to be calibrated since its signal is subject to influences other than the impinging light. The sensor signal S can be modeled as a sum of a radiometric signal S_0 ~~between 0–2000 DN it follows the function~~

$$\sigma_\mathcal{N} = \sqrt{0.043 S_0 + 5.07^2}\ \text{[DN]}.$$

For larger values the noise variance $\sigma^2_{\mathcal{N}}$ no longer scales linearly with $\langle S_0 \rangle$ but remains below the fit in Eq. (13). As seen in Fig. (13) bottom left, the VNIR noise can no longer be explained by a Poisson noise model (Eq. 12) with a constant conversion gain k [DN]. This noise characteristic can be an indication for two different mechanisms at work. Either k [DN] varies with signal level containing only radiance information, S_d which describes the dark signal of the sensor and the noise $\mathcal{N}$ of the sensor:

$$S = S_0 + S_\mathrm{d} + \mathcal{N} \tag{1}$$

In the following subsections dark signal S_d, radiometric signal S_0 , which would cause a photon response nonlinearity (PRNL) or a charge sharing is occurring between pixels which would violate the Poisson assumption. A more in-depth analysis of the noise showed a small autocorrelation within pixels of the same spatial sensorrow, which would suggest the latter. But as the PRNL analysis in Sect. **??** will show, radiometric nonlinearity has to be considered as well as a possible explanation.

In contrast the SWIR noise standard deviation $\sigma_{\mathcal{N}}$ shown in Fig. 13, top right compares much better to the Poisson model. Between 0–12000 DN it fits the following form:

$$\sigma_{\mathcal{N}} = \sqrt{0.015 S_0 + 4.77^2}\ \text{[DN]}$$

At larger values of $\langle S_0 \rangle$ the noise variance $\sigma^2_{\mathcal{N}}$ remains linear with $k = 0.015$ [DN] until saturation is reached. For both sensors no wavelength dependence in noise was foundand noise $\mathcal{N}$ will be independently examined. In the remaining subsections optical performance like angular and spectral bandwidth as well as keystone effects will be discussed.

3.1.1 Dark signal

Inherent to all electronic imaging sensors is the dark signal S_d. It is a pixel dependent offset and its variation between pixels is often described as dark signal non-uniformity. The total

signal S is composed of the photoelectric signal S_0, a dark signal S_d and the remaining noise $\mathcal{N}$ (Eq. 1). When the shutter is closed and ~~subsequently~~ the photoelectric signal ~~$S_0 = 0$~~ S_0 becomes zero by definition, an averaged ~~$\langle S_\mathrm{d} \rangle$~~ dark frame $\langle S_\mathrm{d} \rangle$ with very small remaining noise (as $\langle \mathcal{N} \rangle \to 0$) can directly be measured~~as $\langle \mathcal{N} \rangle \to 0$~~:

$$\langle S \rangle = \langle S_0 + S_\mathrm{d} + \mathcal{N} \rangle = \langle S_\mathrm{d} \rangle + \langle \mathcal{N} \rangle \approx \langle S_\mathrm{d} \rangle \tag{2}$$

The dark signal S_d is further composed of the dark current signal $S_\mathrm{dc} = s_\mathrm{dc} t_\mathrm{int}$ and ~~the~~ a readout offset S_read:

$$S_\mathrm{d} = s_\mathrm{dc} t_\mathrm{int} + S_\mathrm{read} \tag{3}$$

The dark current s_dc ~~is also known as reverse leakage current and is a characteristic of all diodes. It~~ originates from thermally generated electrons and holes within the semiconductor material. Since the electrons are randomly generated over time, the dark current signal S_dc increases linearly with s_dc and integration time t_int. The remaining offset S_read is caused by the readout process and is therefore independent from t_int.

The dark signal $S_\mathrm{d}(t_0)$ of an illuminated frame at time t_0 is estimated through linear interpolation of averaged dark frames $\langle S_\mathrm{d}(t_{-1}) \rangle$ and $\langle S_\mathrm{d}(t_1) \rangle$ measured at t_{-1} before and t_1 after the image frame:

$$\langle S^*_\mathrm{d}(t_0) \rangle = (1-w) \langle S_\mathrm{d}(t_{-1}) \rangle + w \langle S_\mathrm{d}(t_1) \rangle \qquad \text{with:} \quad w = \frac{t_0 - t_{-1}}{t_1 - t_{-1}} \tag{4}$$

The photoelectric signal $S_0(t_0)$ (including the remaining noise $\mathcal{N}$) can then be estimated using the interpolated dark frame $\langle S^*_\mathrm{d}(t_0) \rangle$:

$$S_0(t_0) + \mathcal{N} = S(t_0) - S_\mathrm{d}(t_0) \approx S(t_0) - \langle S^*_\mathrm{d}(t_0) \rangle. \tag{5}$$

Hereby, the linear interpolation leads to a dark signal uncertainty

$$\sigma_\mathrm{d}(t_0) = \sqrt{\sigma^2_\mathrm{d}(t_{0-})(1-w) + \sigma^2_\mathrm{d}(t_{0+})w}. \tag{6}$$

This uncertainty results from standard deviations $\sigma_\mathrm{d}(t_{+1})$ and $\sigma_\mathrm{d}(t_{-1})$ of the individual dark signal averages at t_{-1} and t_1 in combination with an upper estimate for the dark signal drift $\Delta\overline{S_\mathrm{d}}$ projected forward from t_{-1} and backward from t_1 to time t_0:

$$2\sigma_\mathrm{d}^2(t_{0-}) = 2\sigma_\mathrm{d}^2(t_{-1}) + \left(\Delta\overline{S_\mathrm{d}}(t_0 - t_{-1})\right)^2$$

$$2\sigma_\mathrm{d}^2(t_{0+}) = 2\sigma_\mathrm{d}^2(t_1) \pm \left(\Delta\overline{S_\mathrm{d}}(t_1 - t_0)\right)^2$$

To specify this uncertainty for actual measurements, the following analysis will investigate the dark signal characteristic, e.g. the maximal dark signal drift, of both sensors.

The dark signal analysis was done under controlled laboratory conditions during calibration within the CHB facility as well as on one flight during the ACRIDICON-CHUVA campaign. In order to suppress the noise during lab analysis, 500 consecutive dark frames were averaged. Dark frames were measured for 9 different integration times while ambient air temperatures were held constant by air-conditioning. During the measurements the temperature in the VNIR casing remained stable at 312.0 K. Since the SWIR camera is not equipped with a temperature sensor the VNIR temperature has been used as a proxy.

For the analysis during the flight only 30 consecutive dark frames were averaged to minimize gaps between radiometric measurements. Analysis of mean dark signal levels $\overline{S_\mathrm{d}}$ inflight over all pixels was done for both spectrometers using integration times t_int of 5, 8, and 12 ms. During the 6 h flight the ambient air temperature was gradually changing due to the cabin air-conditioning system. This led to fluctuating VNIR casing temperatures between 312.4 and 320.6 K.

The ~~typical variation of dark signals within a minute can be up to 10 DN. As data can be captured substantially faster, the dark signal S_d of an illuminated frame can be estimated through interpolation of dark frames measured before and/or after the image frame. Using the interpolated dark frame $\langle S_\mathrm{d}^* \rangle$, the photoelectric signal (including the remaining noise) $S_0 + \mathcal{N}$ can be estimated:~~

$$S_0 + \mathcal{N} = S - S_\mathrm{d} \approx S - \langle S_\mathrm{d}^* \rangle.$$

The analysis of the dark signal shows clear differences between the sensors used for the VNIR and the SWIR spectrometer. Figure 6 (right) shows mean dark signal levels $\overline{S_\mathrm{d}}$ in available digital number range when averaging over 30 dark frames as measured during a flight of the aircraft campaign ACRIDICON-CHUVA. The green curve shows the readings from a temperature sensor located within the casing of the VNIR spectrometer. While the level of $\overline{S_\mathrm{d}}$ for the SWIR depends on integration time t_int as well as on temperature, the level of $\overline{S_\mathrm{d}}$ for the VNIR seems independent from t_int and temperature. The typical variation of the dark signal within a minute was around 10 DN Maximal dark current drifts $\Delta\overline{S_\mathrm{d}}$ of 30 DN/min were found for the SWIR and 3 DN , while $\Delta\overline{S_\mathrm{d}}$ remained below 6 DN/min for the VNIR. In the following, these values will be used as upper estimate in the calculation of the 2σ error of the dark signal in Eq. 6.

A more in-depth analysis of this the dark signal behavior is shown in Fig. 6 (left) where measurements of S_d in a controlled lab environment (CHB) are compared with measurements of S_d during the mentioned flight. The slope of the regression line reflects the dependence of $\overline{S_\mathrm{d}}$ on t_int while the shaded area shows the influence of temperature on this relationship. In Fig. 6 (left) the non-uniformity of S_d is shown by error bars, which is only significant in the case of for the SWIR. With temperature increasing from 310.4 to 320.0 K the number of thermally generated electrons per second increases from 352 DN ms^{-1} to 494.0 DN ms^{-1} for the SWIR sensor. In this temperature range the VNIR sensor shows only a marginal influence on dark signal levels. In contrast, a considerable amount of dynamic range is lost to the dark signal in the case of for the SWIR.

In the case of the VNIRFor the VNIR, there is mainly a fixed dark signal offset independent of t_int. Since thermally generated electrons do not play an important role in dark signal generation within the VNIR sensor the independence of S_d from t_int and temperature is evident. In order to push the dark signal below the photoelectric signal the HgCdTe-based detector of the SWIR spectrometer has to be cooled down to 200 K. Although the SWIR sensor is equipped with a thermoelectric cooler the dark signal S_d in Fig. 6 is obviously still influenced by air temperature fluctuations.

Additionally, dark signal offsets S_{read} exhibit a slight dependence on temperature in both spectrometers. The offsets S_{read} between both sensors differ fundamentally with respect to their pixel-wise distribution and the fixed pattern noise they are creating. Figure 9 shows the noticeable uneven fixed pattern noise FPN^{SWIR} of the SWIR sensor. While FPN^{VNIR} appears smooth with $\sigma_{\text{FPN}}^{\text{VNIR}} = 9.4\,\text{DN}$ the spatial distribution of FPN^{SWIR} is very uneven with $\sigma_{\text{FPN}}^{\text{VNIR}} = 173.8\,\text{DN}$. ~~Figure 9 shows FPN^{SWIR}.~~ Bad pixels that were excluded in this analysis are also shown. ~~Without correction of this offset by subtraction of a promptly measured dark frame the spectral as well as the spatial SWIR measurements would be strongly biased.~~

3.1.2 Nonlinear radiometric response

The photoelectric signal ~~$S_0^* \tilde{S}_0$~~ from a perfectly linear sensor with response R should scale linearly with ~~integration time t_{int}~~ the set integration time t_{set} and radiance L:

$$S_0^* \tilde{S}_0 = RLt_{\text{set}} = s_{\text{n}} t_{\text{int}} \propto Lt_{\text{int}} \cdot t_{\text{set}} \tag{7}$$

Accordingly, there exists an unambiguous normalized signal ~~s_{n}~~ $s_{\text{n}} = RL$ independent from camera ~~parameters~~ settings for each radiance value L. However, measurements of constant radiance levels originating from a large integrating sphere (LIS) with various integration times (see Table 2) have shown deviations from ~~the~~ this idealized linear model ~~in Eq. 7.~~

~~This deviation~~. This deviation between the idealized signal $\tilde{S}_0$ and the actually observed signal S_0 is called photo response non-linearity ~~(PRNL). The~~. Figure 7 and 8 show the found deviations of the VNIR and SWIR from the idealized linear model (Eq. 7). Here, the photoelectric signal S_0 of the same stabilized light source (LIS) should become invariant after normalization with the set integration time t_{set}. The fit of the original VNIR signal s_{n} (grey line, Fig. 7) seems to show a photo response non-linearity, which is visible at higher signal levels by lower DN for $t_{\text{set}} = 12.0\,\text{ms}$ compared with $t_{\text{set}} = 2\,\text{ms}$. By contrast, the fit of the original SWIR signal s_{n} (grey line, Fig. 8) is almost linear but seems to be insufficiently

normalized when using the set integration time t_{set}. To obtain absolute radiance values, the photoelectric signal S_0 has to be linearized first before the absolute radiometric response can be applied~~to yield absolute radiance values~~. In the following, the different deviations of both sensors from the linear model (Eq. 7) will be analyzed in detail.

We identified two effects which together explain the observed nonlinearities very well. According to Janesick (2007) the diode capacitance of CMOS detectors can increase significantly as charge collects. Thereby the sensor specific conversion gain k [DN] becomes a function of the number N of received photoelectrons. For higher signal levels this causes a nonlinear relationship between incoming radiance L and the photoelectric signal S_0. We considered this nonlinearity by adding a quadratic term to Eq. (7), which leads to the form in Eq. (8). Furthermore we found a small mismatch between the ~~integration time set~~ set integration time t_{set} and the actual integration time t_{int}. For this reason, an offset term t_{ofs} was added to be fitted in the model in Eq. (8).

~~The~~ The improved model which describes the observed photoelectric signal S_0 then reads:

$$S_0 = s_{\mathsf{n}}(t_{\mathsf{set}} + t_{\mathsf{ofs}}) + \gamma\,(s_{\mathsf{n}}(t_{\mathsf{set}} + t_{\mathsf{ofs}}))^2 \tag{8}$$

Here, γ is the nonlinearity of S_0 in DN^{-1} and t_{ofs} is the offset between actual and reported integration time. The model can be inverted to yield the normalized signal s_{n} from measured signal S, dark signal S_{d} and t_{set} when γ and t_{ofs} are known:

$$s_{\mathsf{n}} = \frac{\sqrt{4\gamma(S - S_{\mathsf{d}}) + 1} - 1}{2\gamma(t_{\mathsf{set}} + t_{\mathsf{ofs}})} \xrightarrow{\gamma \to 0} \frac{S - S_{\mathsf{d}}}{t_{\mathsf{set}} + t_{\mathsf{ofs}}} \tag{9}$$

This nonlinear model converges to the linear model in Eq. (7) for $\gamma \to 0$ and $t_{\mathsf{ofs}} \to 0$.

Using the integration times in Table 2 and the model described in Sect. 3.1.2, the parameters γ and t_{ofs} were determined for every pixel. This was done for measurements taken on the large integrating sphere at the CHB facility on 3 July 2014 by regression of measured S_0 on Eq. (8) using the least squares method. Since solar radiances are naturally very strong

signals the model in Eq. (8) was not designed to model effects at very low signal levels. For this reason the fit was only done for pixels with signal levels higher than 2 % of the maximum signal level. Mean and standard deviation of γ and t_{ofs} over the sensor are shown in Table 3. The fact that γ and t_{ofs} do not vary much across pixels allows ~~the general applicability of this values to all pixels~~ to use a single value for each of them on the whole sensor for simplicity. As the agreement between the presented model and all measurements was very good, a possible further dependence of the model parameters on other parameters has been discarded.

For the VNIR camera the nonlinearity causes a deviation of 9 % from the linear model at maximum signal level while the SWIR camera does not exhibit a noticeable nonlinearity. In contrast t_{ofs} of the VNIR camera is negligible with $0.001\,\text{ms}$ while the SWIR offset $0.055\,\text{ms}$ lies within the same order of magnitude as the shortest possible integration time of $0.1\,\text{ms}$.

By using the found parameters γ and t_{ofs} in the nonlinear model (Eq.), the linearized signal s_{n} of the VNIR is shown by the blue line in Fig. 7, while s_{n} of the SWIR is shown by the red line in Fig. 8. After the nonlinearity correction, the VNIR signal s_{n} better follows the linear model. Likewise, the corrected SWIR signal s_{n} now seems sufficiently normalized by using the additional integration time offset t_{ofs}.

Hereby, the uncertainty in γ and t_{ofs} leads to a remaining nonlinearity uncertainty σ_{nonlin}. The maximum error due to this uncertainty was estimated by using the error boundaries of both parameters in Eq. 3.1.2. Hereby, only the uncertainty in γ for the VNIR is of significance which is shown by the blue filled area in Fig. 7.

During this analysis, some alternate nonlinearity models have been considered to improve the confidence in the existing nonlinearity parameterization, which is assumed to be a function of total collected radiative energy ($\propto L \cdot t_{\text{int}} \propto s_{\text{n}} \cdot t_{\text{int}}$). A simpler model, considering only a quadratic term in t_{int}, was not able to provide similarly good results as the model presented above. Some combinations of quadratic or higher order terms in the form of $s_{\text{n}}^{a} \cdot t_{\text{int}}^{b}$ have also been tried, assuming equal nonlinear response of all pixels of one sensor and exploiting the intensity variations between pixels as introduced by the spectrograph. As the assumption of equal nonlinear response for all pixels has been found

to hold true for the finally chosen model and neither of the alternate models showed better results, they have also been discarded. This behaviour suggests, but is no evidence, that the signal is actually a nonlinear function of the total collected radiative energy and neither in t_{int} nor L alone.

3.1.3 Absolute radiometric response

After nonlinearity correction the normalized signal s_{n} in [DN ms^{-1}] can be converted into absolute radiance values L in [mWm^{-2}nm^{-1}sr^{-1}]. Using the absolute radiometric response R in [DN ms^{-1}mW^{-1}m^{2}nm sr], this can be described by

$$L = R^{-1} \cdot s_{\mathrm{n}}. \tag{10}$$

R is different for each pixel and thereby also covers the correction of inter-pixel variations of the sensor response, also called photo response non-uniformity (PRNU). The absolute radiometric response R is determined once during a radiometric calibration with a known radiance standard.

In this work the absolute radiometric response R was characterized using the absolute RAdiance STAndard (RASTA) (Schwarzmaier et al., 2012) of the IMF at DLR-EOC which was characterized with absolute radiance standards operated by the PTB (~~Physical. Techn.~~ Physikalisch-Technische Bundesanstalt), the German National Metrology Institute. As the RASTA does not cover the full field of view of the sensors, a large integrating sphere (LIS) was additionally used as an isotropic light source. As determined by Baumgartner (2013) , the output stability of the LIS is better than $\sigma = 0.02\,\%$ for a duration of 330 seconds.

To transfer the absolute radiance standard from the RASTA to the LIS, measurements of both light sources were performed in fast succession with pixels in the geometric center of the specMACS FOV. The absolute calibration of the RASTA can then be transferred to the LIS by using the ratio between the normalized signals $s_{\mathrm{n;LIS}}$ and $s_{\mathrm{n;RASTA}}$ measured at the integrating sphere and the absolute standard:

$$L_{\mathrm{LIS}} = L_{\mathrm{RASTA}} \cdot \frac{L_{\mathrm{LIS}}}{L_{\mathrm{RASTA}}} = L_{\mathrm{RASTA}} \cdot \frac{s_{\mathrm{n;LIS}}}{s_{\mathrm{n;RASTA}}} \tag{11}$$

Simultaneously the calibration transfer was done with a second, independent spectrometer (SVC HR-1024i) to validate the transfer with the specMACS instrument.

~~Using Eq. 11 the calibration was transferred from the absolute radiance standard RASTA to~~ In Fig. 10 the spectral radiance of the large integrating sphere ~~for both specMACScameras and a third spectrometer (SVC-HR1024i)independently from each other.~~ is shown as it was transferred from the RASTA standard using Eq. (11).

With the LIS illuminating the complete FOV of the instrument the conversion from normalized signals to absolute radiances (R in Eq. 10) is calculated for each pixel.

The absolute radiometric response R of the VNIR and the SWIR ~~camera~~ sensors are presented in Fig. 11. Both sensors show strongly reduced sensitivity at the upper and lower boundaries of the spectrum, which is expected due to the nature of the material dependent band-gap and the transmissivity of the optical system. The VNIR sensor shows an etalon fringe pattern (seen in Fig. 11(left) along the spectral dimension) typical for backside-illuminated sensors (Marques Vatus and Magnan, 2004), whereas the front-illuminated SWIR sensor does not exhibit significant patterns. The discrepancy between the found absolute radiometric responses R and the ones given by the manufacturer does not exceed more than 10 %.

~~In Fig. ??a the spectral radiance of the large integrating sphere is shown as it was transferred from the RASTA standard using Eq. (11). With the LIS illuminating the complete FOV of the instrument the conversion from normalized signals to absolute radiances (Eq. 10) is calculated for each pixel. This conversion is described by the absolute radiometric response R.~~ Using the nominal accuracies of the reference light sources and signal statistics derived from the sensors during characterization measurements, an error budget for the absolute radiometric response R was calculated and is shown as 2σ uncertainty in Fig. ~~??b~~12. The uncertainty in the absolute radiometric calibration of the RASTA was given by the PTB and is indicated by the green line in Fig. ~~??b~~12. At longer wavelengths the nominal uncertainty of the RASTA increases, which can be traced back to the

accuracy of the reference radiometers used during the RASTA characterization at the PTB. The uncertainty due to inhomogeneities of the LIS is given to be $\pm 1.6\,\%$ (Baumgartner, 2013). Another source of uncertainty arises from the drift of the dark signal S_d over time and from the noise $\mathcal{N}$ of the signal S, which is shown as blue (VNIR) and red (SWIR) dashed lines. The drift per minute was assumed to be $10\,\mathrm{DN}$ ~~in case of~~ for the SWIR and $3\,\mathrm{DN}$ ~~in case of~~ for the VNIR as found in the dark signal analysis (Sect. 3.1.1). The noise was calculated for 100 averaged dark frames and 500 averaged illuminated frames resulting in $\sigma_{\langle S \rangle} = 0.5\,\mathrm{DN}$. At the RASTA and the LIS the 2σ uncertainty due to the dark signal drift and noise accounts to around 1 % ~~in case of~~ for the VNIR and 3 % ~~in case of~~ for the SWIR for wavelengths in the center of both spectra. While the dark signal drift and noise level stays constant with wavelength the radiometric sensitivity and therefore the signal S decreases towards the edges of the spectra. This results in a sharp increase of the relative uncertainty towards spectral regions with low radiometric sensitivity. In particular towards the edges of the spectra, the drift of the dark signal S_d contributes the most to the overall radiometric uncertainty. Altogether this error budget is a very conservative estimate for an individual measurement with a single pixel without any averaging. For relative measurements some of these uncertainties cancel out e.g. the LIS inhomogeneity and the RASTA uncertainty during a window transmissivity characterization presented in Sect. 4.2.1.

3.1.4 Noise

The noise $\mathcal{N}$ is composed of dark current noise $\mathcal{N}_\mathrm{dc}$, read noise $\mathcal{N}_\mathrm{read}$ and photon shot noise $\mathcal{N}_\mathrm{shot}$. Their joint standard deviation $\sigma_\mathcal{N}$ is calculated using the individual standard deviations σ_shot, σ_dc and σ_read:

$$\sigma_\mathcal{N} = \sqrt{\sigma_\mathrm{shot}^2 + \sigma_\mathrm{dc}^2 + \sigma_\mathrm{read}^2} = \sqrt{k^2 N + \sigma_\mathrm{d}^2}. \tag{12}$$

Since photons arrive randomly in time the number N of photoelectrons measured during a fixed time interval is distributed according to the Poisson distribution. Following the Poisson statistics the standard deviation σ_N of a distribution with the expectation value

N is proportional to $\sqrt{N}$. For this reason the photon shot variance σ^2_{shot} scales linearly with the number of incoming photoelectrons N and the squared conversion gain k^2 [DN^2] (Eq. 12). For a sensor with linear response, the relation $S_0 \propto N$ holds. A deviation from this relationship can be an indication for a nonlinear relationship between the number N of photoelectrons and the photoelectric signal S_0 or is caused by a non-Poisson noise source.

Similar to the dark signal S_d in S, a dark noise $\mathcal{N}_\text{d}$ remains in $\mathcal{N}$ without illumination. It is comprised of dark current noise $\mathcal{N}_\text{dc}$ and readout noise $\mathcal{N}_\text{read}$. The dark current noise is caused by statistical variation of thermally generated electrons. Pixel readout and analog to digital conversion is further subject to electronic readout noise, which is independent from integration time.

For this analysis, $\sigma_\mathcal{N}$ is calculated as the pixel-wise standard deviation of 500 consecutive frames which were obtained during the nonlinearity measurements with varying integration times as listed in Table 2. Here, the noise standard deviation $\sigma_\mathcal{N}$ and mean, darkcurrent-corrected signal level $\langle S_0 \rangle$ are calculated individually for each pixel, since both sensors cannot be homogeneously illuminated due to the spectrographic diffraction grating, As noise $\mathcal{N}$ describes unbiased temporal variations of the signal around its expectation value, its temporal mean vanishes: $\langle \mathcal{N} \rangle \approx 0$.

Figure 13 shows the results of the noise analysis. For each pixel and each integration time, the mean and standard deviation was calculated and accumulated in the shown 2-D histograms. The noise characteristics of the VNIR are shown on the left while results for the SWIR are shown on the right. On top in Fig. 13 the pixel-wise standard deviation $\sigma_\mathcal{N}$ is plotted against the mean, darkcurrent-corrected signal level $\langle S_0 \rangle$ on a log-log scale. On the bottom, the same is done with the pixel-wise variance $\sigma^2_\mathcal{N}$ on a linear scale.

With the classic Photon Transfer Curve (PTC) (Janesick, 2007) the noise characteristics can be used to determine many important camera parameters. When the signal noise standard deviation $\sigma_\mathcal{N}$ is plotted against the mean, darkcurrent-corrected signal level $\langle S_0 \rangle$ on a log-log scale, like it is done in Figure 13, different noise regimes become apparent. The dark noise at integration time $t_\text{int} = 0\,\text{s}$ at the lower end of $\langle S_0 \rangle$ is

dominated by read-out noise with standard deviation σ_{read}. With increasing mean signal level $\langle S_0 \rangle$ photon shot noise becomes dominant with σ_{shot}. Due to the Poisson-like distribution the photon shot noise variance σ^2_{shot} should scale linearly with mean signal level. Deviations from this linear relationship can provide an indication of a nonlinear radiometric response (Bohndiek et al., 2008) or a charge sharing mechanism between pixels (Downing et al., 2006; Stefanov, 2014) .

At low values of $\langle S_0 \rangle$ the signal-independent read-out noise becomes apparent. The read-out noise for $t_{\text{int}} = 0\,\text{s}$ is derived as the y-intercept of a constant fit on $\sigma_{\mathcal{N}}$ for $\langle S_0 \rangle < 30\,\text{DN}$. By doing this, the noise associated with the readout channel was found to be 5.0 DN for the VNIR and 4.5 DN for the SWIR spectrometer. For larger values of $\langle S_0 \rangle$ the noise begins to increase.

When the standard deviation $\sigma_{\mathcal{N}}$ is fitted with the square root model following Eq. (12), the noise characteristics can be further investigated. At first glance, the noise standard deviation of the VNIR sensor is in accordance with the noise model described by Eq. (12) with a constant conversion gain $k = 0.043\,[\text{DN}]$. For values of S_0 between 0–2000 DN it follows the function

$$\sigma_{\mathcal{N}} = \sqrt{0.043 S_0 + 5.07^2}\ [\text{DN}]. \tag{13}$$

For larger values the noise variance $\sigma^2_{\mathcal{N}}$ no longer scales linearly with $\langle S_0 \rangle$ but remains below the fit in Eq. (13). As seen in Fig. (13) bottom left, the VNIR noise can no longer be explained by a Poisson noise model (Eq. 12) with a constant conversion gain $k\,[\text{DN}]$. This noise characteristic can be an indication for two different mechanisms at work. Either $k\,[\text{DN}]$ varies with signal level S_0, which would cause a photon response nonlinearity or a charge sharing is occurring between pixels which would violate the Poisson assumption. A more in-depth analysis of the noise showed a small autocorrelation within pixels of the same spatial sensor row, which would suggest the latter. But as the photon response nonlinearity analysis in Sect. 3.1.2 has shown, radiometric nonlinearity has to be considered as well as a possible explanation.

In contrast the SWIR noise standard deviation σ_N shown in Fig. 13, top right compares much better to the Poisson model. Between 0–12 000 DN, which is only limited by the subtracted dark signal, it fits the following form:

$$\sigma_N = \sqrt{0.015 S_0 + 4.77^2}\ \text{[DN]} \tag{14}$$

At larger values of $\langle S_0 \rangle$ the noise variance σ_N^2 remains linear with $k = 0.015$ [DN] until saturation is reached. For both sensors no wavelength dependence in noise was found.

3.1.5 Polarization sensitivity

All optical components can exhibit polarization dependent loss, which in effect makes the signal sensitive to polarization. This polarization sensitivity has an influence on the absolute radiometric response R when parts of the measured light are linearly polarized. ~~To investigate this influence~~The polarization sensitivity can be examined by splitting the instrument response virtually into a polarization insensitive part with partial response O and a fully polarization sensitive part with partial response $2A$, such that $R = A + O$ for unpolarized light. In line with Malus' Law the polarization dependent normalized photoelectric signal $s_n^P(\phi)$ of incoming radiance L, with a degree of polarization p, measured with such an instrument is given by

$$s_n^P(\phi) \eqsim 2A \cdot L_\parallel + O \cdot L \tag{15}$$

$$\eqsim 2A \left(p \cos^2(\phi - \phi_0) + \frac{1-p}{2} \right) \cdot L + O \cdot L \tag{16}$$

Here, $L_\parallel$ denotes the incoming radiation parallel to the sensors polarization direction, ϕ the polarization orientation with respect to the entrance slit and ϕ_0 the polarization orientation for which $s_n^P(\phi)$ is maximal.

To investigate the polarization influence, a wide-band wire grid polarizer (99.9% degree of polarization between ~~400–2500~~400 – 2500 nm) mounted in a rotation stage was placed

between the large integrating sphere and the specMACS instrument. Following Lenhard et al. (2015), measurements of the photoelectric signal ~~$S_0(\phi)$~~ ~~$s_n^P(\phi)$~~ were done while rotating the polarizer between 0° and 180° with respect to the entrance slit in steps of 15°. ~~In line with Malus' Law the photoelectric signal $S_0(\phi)$ of perfectly polarized light measured with a polarization sensitive instrument is given by~~

~~$$S_0(\phi) = A \cdot \sin^2(\phi - \phi_0) + O$$~~

~~Here ϕ is the angular orientation of the polarizer,~~ For fully polarized light ($p = 1$) of intensity L, Fig. 14 shows the polarization sensitive behavior of $s_n^P(\phi)$ for one VNIR pixel (spatial: 400, spectral: 600) while rotating the wire grid polarizer (red crosses). While the maximum of $s_n^P(\phi)$ can be found for polarization orientations parallel to ϕ_0, the maximum signal loss due to the polarization sensitivity occurs orthogonal to ϕ_0

In the following, the ~~angular orientation for which $S_0(\phi)$ is minimal, A the amplitude of the polarization sensitive signal part and O the~~ polarization sensitivity P is defined as the increase of the signal between unpolarized light ($p = 0$) and light fully polarized in the most sensitive direction of the sensor ($p = 1, \phi = \phi_0$), while the total radiance of the light source remains unchanged. The polarization sensitivity P reads as follows:

$$P = \frac{A}{A + O} \cdot 100\,\% \tag{17}$$

A natural light source has an unknown degree p and orientation ϕ of polarization. Nonetheless, the maximum error in the normalized signal s_n due to polarization can be given for an estimated maximum degree of polarization $p_{max} \leq 1$. Note that this estimate is always possible in the form of $p_{max} = 1$ for a completely unknown light source. Following Eq. 16, any signal s_n^P measured from an incoming radiance L with maximum degree of polarization p_{max} can be constrained for the following bounds (which are illustrated by the red shaded region in Fig. 14):

$$((1 - p_{max})\,A + O)\,L \leq s_n^P \leq ((1 + p_{max})\,A + O)\,L \tag{18}$$

Ideally, the signal would be independent from ϕ, following the linear model $s_n = RL$. In particular, this holds true for s_n^P for unpolarized light ($p_{max} = 0$), as it was the case during the radiometric characterization. It follows that the error Δs_n for an unknown degree $p > 0$ and orientation ϕ of polarization is given by $\Delta s_n = |s_n - s_n^P|$. An upper bound of the error Δs_n due to polarization ~~insensitive signal offset. When the measurements with the rotating polarizer are fitted to the model in Eq. (16)the~~ can then be estimated by using $s_n = RL$, $R = A + O$ and Eq. 18:

$$\Delta s_n \leq \max\left(\left|RL - \left(\left(1 \pm p_{max}\right) A + O\right) L\right|\right) = p_{max} AL \tag{19}$$

Furthermore, an upper bound for the relative uncertainty due to polarization can be estimated using the polarization sensitivity P ~~can be determined as the ratio between the polarization sensitive signal amplitude~~ by estimating L through s_n^P using Eq. 18 again and inserting Eq. 17 after solving for A~~and the polarization insensitive signal offset O~~:

$$P = \frac{A}{O} \cdot 100\,\%$$

~~The maximum signal loss due to the polarization sensitivity then occurs at the angular offset ϕ_0 with respect to the entrance slit.~~

$$\frac{\Delta s_n}{s_n^P} \leq \frac{p_{max} A}{(1 - p_{max}) A + O} = \frac{p_{max} P}{1 - p_{max} P} \tag{20}$$

In the field, radiation is never fully polarized. The polarization of sunlight reflected by water clouds is well below 5 % for most viewing geometries. It only reaches values of up to 15 % in the rainbow region of optically very thin clouds (Hansen, 1971) . In contrast, Rayleigh scattering can be strongly polarized, depending on the scattering angle. If strongly polarized light must be assumed, the calibrated radiance has to be handled with care and provided with corresponding uncertainty estimates following Eq. 20. For sensor regions with a small

polarization sensitivity P, the relative radiometric error due to polarization scales linearly with the light polarization p.

~~The results of the polarization sensitivity measurement are shown in Fig. 15.~~ The polarization sensitivity P and the angular offset ϕ_0 were found by fitting ~~measurements of light with different polarization angles~~ the measurements to Eq. ~~(16). For the VNIR on the left and for the SWIR on the right,~~ 16. In Fig. 15~~shows the polarization sensitivity P for all pixels. With the entrance slit oriented horizontally in Fig. 15 the angular offset~~ , the characterization results for P and ϕ_0 ~~is indicated by~~ are shown as color and black lines respectively. Here, the black solid lines ~~. For this polarization orientation the polarization dependent signal loss becomes maximal for the particular pixel. For real measurements, when the polarization degree and orientation is unknown, the maximum radiometric error is given by $P/2$~~indicate the polarization orientation for which the signal becomes minimal. The polarization sensitivity P can be observed to increase from ~~2 to 10~~1% to 5% towards larger wavelengths for both cameras, resulting in a maximum error of 5.3 % for fully polarized light. While P is higher in the center of the VNIR FOV, it increases towards the edges ~~in case of~~ for the SWIR. Furthermore very high values for P (~~$> 10\%$~~$> 5\%$) can be observed at both wavelength cutoffs of the SWIR, where the radiometric sensitivity becomes very small. Due to the very low radiometric sensitivity of the SWIR the region of shortest wavelengths were excluded in this analysis. ~~The~~ Despite the slightly different definition, the values of P agree well with Lenhard et al. (2015) and Hyvarinen et al. (1998) and can be explained by the polarization caused at the entrance slit and the holographic transmission grating.

3.1.6 Overall radiometric uncertainty budget

To specify the total radiometric uncertainty for every measurement, the following section will give a bottom-up calculation of the propagation of radiometric errors. As it has already been done during the estimation of the total dark signal uncertainty, maximum errors (Δ) are being used as approximation of 2σ errors, when no standard deviation is available.

First, the absolute error contibutions to the photoelectric signal S_0 are combined:

$$2\sigma_{S_0} = \sqrt{(2\sigma_{\mathrm{d}}(t_0))^2 + (2\sigma_{\mathcal{N}}(S_0))^2} \tag{21}$$

Here, $\sigma_{\mathrm{d}}(t_0)$ denotes the estimated standard deviation of the dark signal (following Eq. 6) and $\sigma_{\mathcal{N}}(S_0)$ is the estimate of the instantaneous noise of the signal (derrived from the photon transfer curve). Subsequently, the relative error of the normalized signal is obtained by combining the relative errors of the photoelectric signal σ_{S_0} with the estimated remaining nonlinearity uncertainty σ_{nonlin} and the polarization uncertainty Δs_{n}:

$$\frac{2\sigma_{s_{\mathrm{n}}}}{s_{\mathrm{n}}} = \sqrt{\left(\frac{2\sigma_{S_0}}{S_0}\right)^2 + \left(\frac{2\sigma_{\mathrm{nonlin}}}{s_{\mathrm{n}}}\right)^2 + \left(\frac{\Delta s_{\mathrm{n}}}{s_{\mathrm{n}}^{\mathrm{P}}}\right)^2} \tag{22}$$

Lastly, radiometric calibration additionally adds the uncertainty $\frac{\sigma_R}{R}$ of the sensor response:

$$\frac{2\sigma_L}{L} = \sqrt{\left(\frac{2\sigma_{s_{\mathrm{n}}}}{s_{\mathrm{n}}}\right)^2 + \left(\frac{2\sigma_R}{R}\right)^2} \tag{23}$$

An example of typical total uncertainty values for real measurements is given later in the application section (Sec. 4.2.1).

3.2 Spatial and spectral characterization

Besides the radiometric characterization of the spectrometer its spatial and spectral projection onto the detector are of great importance for the scientific application. The radiance contribution for a single pixel from different solid angles is described by two line spread functions (LSF), the across- and along-track LSFs. The spectral responsivity for every pixel is described by a spectral response function (SRF). Moreover some of the pixels of the detector yield unreliable (dead pixel) or biased (hot pixel) measurements, which should be marked and classified as “bad”.

3.2.1 Bad pixel correction

Bad pixels are pixels which do not behave according to the instrument model assumed by the calibration procedure. As already argued by Lenhard et al. (2015), bad pixel characterization of an assembled hyperspectral sensor is not straight forward as a uniform illumination of the sensor chip is not achievable due to the dispersing element. It was decided to manually observe measured data and keep track of pixels which do obviously behave very different from surrounding pixels in a list associated with the calibration files. For the VNIR sensor, there existed no previous knowledge about bad pixels. For the SWIR sensor, the manufacturer provided list of bad pixels was included. Currently one bad pixel is known for the VNIR sensor and 264 randomly distributed bad pixels are known for the SWIR sensor.

Bad pixel correction or the replacement of invalid pixel values by interpolated values is needed if further processing algorithms ~~can not~~ cannot handle invalid pixels in the resulting dataset. Depending on the goal of the proceeding analysis, different interpolation schemes may be appropriate. Currently, bad pixel correction is implemented based on the list of bad pixels provided by the calibration file and a user defined strategy how interpolation rules should be derived from the bad pixel list. The primarily used strategy is to perform a linear interpolation from spatially adjacent good pixels over a single or a group of bad pixels in order to keep spectral features intact.

3.2.2 Response function

Fig. 16 shows a measured line spread function of the VNIR spectrometer and a spectral response function of the SWIR spectrometer. Due to asymmetric distortions of the LSFs of both sensors and the SRFs of the SWIR sensor a fit with a Gaussian function G would yield distorted estimates of center and resolution. For this reason~~a third order B-spline fit F is used~~ , the process to retrieve the center and the resolution respectively bandwidth of the response functions ~~. The~~ is twofold: First, a third order B-spline F is fitted to the measurements to determined the center of a response function ~~is determined by~~ as the median x_c of F.

~~The~~ Then, the resolution Δx is centered around x_c and determined by the area under the normalized spline fit F, which is equal to the area (0.7610) under a Gaussian function $G(x)$ between its full width half maximum FWHM. This way a measure of the response function width is provided in analogy to the full width ~~half-maximum (FWHM)~~ half maximum of a Gaussian shaped function. Consequently~~the resolution Δx can be derived using~~, the resolution is derived by optimizing the symmetric integration limits $\Delta x/2$ to satisfy Eq. 24:

$$\frac{\int_{x_c-\Delta x/2}^{x_c+\Delta x/2} F(x)\,\mathrm{d}x}{\int_{-\infty}^{\infty} F(x)\,\mathrm{d}x} = \frac{\int_{-\mathrm{FWHM}/2}^{\mathrm{FWHM}/2} G(x)\,\mathrm{d}x}{\int_{-\infty}^{\infty} G(x)\,\mathrm{d}x} = 0.7610 \tag{24}$$

~~This~~ The basic idea to transfer the FWHM concept to asymmetric response functions is also illustrated by the inset in Fig. 16~~a~~. Using this technique the angular resolution $\Delta\theta$ and the spectral bandwidth $\Delta\lambda$ are determined.

3.2.3 ~~Spatial characterization~~

~~The information about the geometric properties of the spectrometers is contained in the across-~~ In the following, the terms *along track* and *across track* denote directions perpendicular and ~~along-track LSFs, namely the viewing angles θ_c and the angular resolution $\Delta\theta$. As already defined in the beginning along-track means perpendicular to the instrument spatial slit while across-track means~~ parallel to the spatial ~~slit.~~ line respectively.

3.2.3 Spatial characterization

Every pixel of the sensor arrays has its ~~set of individual LSFs~~own set of LSFs, which are described by the viewing angle θ_c and the angular resolution $\Delta\theta$. The viewing angles θ_c of one spatial pixel along the spectral axis are ideally the same. Any deviation is commonly called keystone, which is expressed as the maximum difference of the viewing angles of one spatial pixel. The width of LSFs $\Delta\theta$ across- and along-track determines the sharpness of the spatial image.

The geometric and spectral characterizations were done analogous to Gege et al. (2009) and Baumgartner et al. (2012). The measurement setup consists of a narrow slit with a width of 0.05 mm, illuminated by a Quartz Tungsten Halogen lamp and positioned at the focal plane of a reflective collimator with a focal length of 750 mm. This results in a collimated beam with a divergence of 0.07 mrad that is guided via a folding mirror onto the aperture of the spectrometer. Through linear movement and simultaneous rotation of the folding mirror, different spatial pixels can be illuminated. The collimated beam is large enough to fill the aperture of the spectrometer.

The across-track LSFs are measured by using a slit which is imaged perpendicular to the entrance slit of the spectrograph. The angular scan for the selected pixels is accomplished by changing the illumination angle via the folding mirror over a range of 0.7 rad. For the VNIR this scan is done in increments of 0.14 mrad covering the entire FOV. In case of the SWIR instrument, the scan is performed in increments of 0.35 mrad.

The along-track LSFs are measured at 7 angles that are evenly distributed over the FOVs of the instruments. They are measured by using a slit that is imaged parallel to the entrance slit of the spectrograph. The incidence angle of the collimated beam on the spectrometer aperture is changed by a along-track translation of the illuminated slit in the focal plane of the collimator. For the measurement of the selected spatial pixels of the VNIR, the along-track LSF is scanned over a range of 6.06 mrad in increments of 0.3 mrad, and for the SWIR over a range of 5.9 mrad in increments of 0.15 mrad.

To retrieve the viewing angles and angular resolutions from the measurements, the ~~measured data was~~ measurements were interpolated using splines as described in Sect. 3.2.2. The geometric along track values of pixels that are not measured directly are inferred by interpolation of the viewing angles and angular resolution in between the measured spatial pixels. For the interpolation a second order polynomial fit to the measured spatial pixel is used. The order of the polynomial functions is selected so that higher order polynomials do not reduce the residuals significantly more. The keystone distortion of one spatial line is defined as the largest difference of across-track viewing angles along the spectral axis.

A typical LSF for the VNIR sensor is ~~show~~ shown in Fig. 16a. As already mentioned in Sect. 3.2.2 the LSFs ~~can not~~ cannot be accurately approximated with Gaussian functions. Therefore splines were fitted to the ~~data~~ measurements to compute the viewing angles θ_c and the angular resolution $\Delta\theta$ of both spectrometers related to the usual FWHM values for a Gaussian shaped sensitivity. The characterization results for both sensors are shown in Fig. 17 and in Tables 4 and 5. Due to low sensitivity some channels of the sensors could not be evaluated accurately. Therefore, the first 30 channels of the VNIR and the first 17 channels of the SWIR sensor are not taken into account. Figure 17a and c show the deviations of the across track viewing angles θ_c relative to spectral channel 400 for the VNIR and to spectral channel 128 for the SWIR sensor. Ripples in Fig. 17a and b are caused by the etalon effect in the VNIR. For both spectrometer the strongest keystone distortion ~~occur~~ occurs at longer wavelengths while its mean value of $0.30\,\mathrm{mrad}$ in the VNIR and $0.50\,\mathrm{mrad}$ in the SWIR remain well below the angular resolution of the sensors.

Figure 17b and d show the across track angular resolution $\Delta\theta$ of the sensors. The area with the smallest $\Delta\theta$ and therefore sharpest pixel is stretched across the sensor FOV. At longer wavelengths and lower pixel numbers the VNIR image projection gets rather blurry. Besides the achromatism this behaviour could be explained by an slightly misaligned entrance slit with respect to the entrance optics. Considering the mean ratio of 3.15 between angular resolution and sampling and the fact that only parts of the image appear sharp the VNIR shows a reduced focusability. The sharpest SWIR image projection is approximately at the center in wavelength but asymmetric in lower pixel numbers as it can be seen in Fig. 17d. With a mean angular oversampling of 1.95 the SWIR optics produce a sharper image on the detector. However, the angular sampling ($1.94\,\mathrm{mrad}$) and resolution ($3.79\,\mathrm{mrad}$) is far coarser than ~~in the case of~~ for the VNIR (0.44 and $1.37\,\mathrm{mrad}$).

The deviations in along track viewing angles θ_c and along track angular resolutions $\Delta\theta$ are not shown here since their values are similar to their across track values. Both along track properties exhibit an even more symmetrical distribution over the sensors.

3.2.4 Spectral characterization

~~To determine the spectral properties of the imaging spectrometers, the spectral response functions (SRF) of the spectral channels need to be characterized.~~ For one spectral channel the SRF center and its width can vary over the FOV of the instrument, i.e. every single pixel of the sensor array has its individual SRF, similar to the LSFs. The deviation of the center wavelength λ_c within a spatial line is commonly described as spectral smile while the SRF width gives the spectral bandwidth $\Delta\lambda$. In the following the spectral smile will be given as the deviation of λ_c with respect to the center pixel within each spatial line.

To measure the SRF, a collimated beam of nearly monochromatic light from a monochromator is used. The collimated beam is guided into the spectrometer's aperture by the already mentioned folding mirror that allows for the illumination of a selectable spatial pixel. A detailed sketch of the calibration setup can be found in Gege et al. (2009) in Fig. 7. To guarantee that the spectrometer aperture and IFOV are completely illuminated, the beam cross-section is larger than the aperture and the beam divergence is larger than the IFOV of the spectrometer. The monochromator has an absolute uncertainty of ± 0.1 nm for wavelengths below 1000 nm, and ± 0.2 nm for longer wavelengths. The spectral bandwidth is set to 0.65 nm for the measurement of the VNIR and 1.3 nm for the measurement of the SWIR. Computations indicate that the chosen bandwidth of the monochromator has only very little influence on the measured bandwidths as long as the monochromator bandwidth is smaller than the measured bandwidth and its SRF is known. With a Gaussian monochromator SRF well below the specified spectrometer bandwidth both requirements are met. For the measurement of the SRFs of the VNIR, the wavelength of the monochromator is scanned from 400 to 1030 nm in steps of 1 nm, and for the SWIR, from 940 to 2550 nm in steps of 2 nm. Due to time constraints, these measurements are only feasible for a small subset of all spatial pixels: For both sensors, the SRFs are measured at seven angles evenly distributed over their across-track FOV.

To determine the two relevant parameters of the SRF, the center wavelength λ_c and the bandwidth $\Delta\lambda$, a Gaussian function is fitted to the data measured for each spectral channel of the VNIR. The center wavelength is then given by the center position of the Gaussian, and the bandwidth as the full width at half maximum (FWHM). For the SWIR a spline is fitted to the data (see Sect. 3.2.2) as the SRFs can not be represented accurately with a Gaussian function as it can be seen in Fig. 16b.

The spectral properties of the other pixels are inferred by fitting the center wavelengths and bandwidths with a second order polynomial. This procedure assumes that the properties of the optical system do not vary rapidly on the scale of the detector array. This assumption holds for the specMACS imaging spectrometers, which was validated using spectral line lamps. The spectral smile for each spatial pixel is computed as the difference between its wavelength and the wavelength of the center pixel within the same spectral channel.

The measurement setup is described in more detail in Gege et al. (2009) and details about the data analysis as well as a validation of the approach for another hyperspectral camera can be found in Baumgartner et al. (2012).

While the SRFs of the VNIR sensor can be reasonably well approximated by Gaussian functions, the SRFs of the SWIR have to be fitted with splines as reasoned in Sect. 3.2.2. The center wavelengths and bandwidths are extracted accordingly. A measured SRF of the SWIR sensor can be seen in Fig. 16b. The figure shows an asymmetric response with a second peak at shorter wavelengths.

The results of the spectral characterization can be seen in Fig. 18 and Tables 6 and 7. As for the geometric characterization some channels are not evaluated. The first 36 channels of the VNIR and the first 17 channels of the SWIR sensor are skipped due to low sensitivity in these regions.

Figure 18a and c illustrate the smile distortion. For the VNIR sensor, the magnitude of the average spectral smile is between 0.1 and 1.1 nm. For the SWIR sensor, the magnitude of the average spectral smile is on the order of 1.1 nm, ranging from 0.1 to 4.1 nm. Note

that the sign of the smile curve changes between the bottom half and the top half of both detector arrays.

Figure 18b and d show the spectral bandwidth of each detector element It is about 3.1 nm in average for the VNIR sensor, and degrades to 6.0 nm at the spatial edges of the detector array. For the SWIR sensor, spectral bandwidth is about 10.3 nm at the center of the detector array, and increases up to 19.6 nm at the spatial edges of the array. ~~In case of the VNIR~~For the VNIR, spectral oversampling is 4.03, which allows the spectral sampling to be reduced by half without losing information. In contrast the average SWIR spectral oversampling is only around 1.64.

The ripple features in the plots of Fig. 18a and b are caused by the etalon effect.

3.2.5 Optical distortion correction

Optical distortion correction can be performed through interpolation of the dataset onto a regular grid. As the adequate grid ~~is problem dependent and~~ depends on the particular application and as interpolation for every pixel is ~~costly in terms of computing power and~~ lossy in terms of information content, this interpolation step should be performed during spatial rectification of the image. Hereby the optical characterization for each instrument is combined with the location ~~data~~ information for each frame, which is then stored together with the radiometric signal from each pixel. Subsequently this meta data can be used in the transformation onto the final target coordinate system.

4 ~~Airborne deployment during ACRIDICON~~Ground-based and airborne applications

~~One of the first~~ First deployments of the ~~full~~ specMACS ~~setup characterised in the previous sections was~~ instrument were the ground-based measurement campaign HOPE in Melpitz, Germany in September 2013 and the aircraft campaign ACRIDICON CHUVA in the Amazon region around Manaus, Brazil in September 2014 (Wendisch et al., 2015). While specMACS was put on a scanning mount during the ground-based campaign, the instrument was

installed on the German research aircraft HALO (High Altitude LOng range aircraft, Krautstrunk and Giez, 2012) ~~for cloud side observations. Additional characteristics specific to this aircraft setup and first results are presented in the next section~~during the ACRIDICON CHUVA campaign.

4.1 Ground-based setup

For ground based measurements, specMACS is mounted on a scanning mount (MESU-OPTICS Mesu-Mount 200) with two rotating axes (vertical and horizontal). This allows the instrument to be pointed anywhere in the upper hemisphere and to perform precise and repeatable automated scans. The scanning mount is equipped with a customized closed loop motor controller (based on a ROBOTEQ Inc., SDC2130). It is equipped with an optical relative position encoder, which allows to control the full turn of each axis in 10 000 steps resulting in a relative positioning accuracy of the angle of about two steps, which is accordingly 0.072° and thereby in the same order as the sensors IFOV.

4.2 ~~Setup on board HALO~~

4.1.1 Ground-based measurements

An exemplary dataset, measured during the ground-based campaign, is given in Fig. 19. The first panel (Fig. 19a) shows a true-color image that was rendered using spectral radiance data from the VNIR camera. Here, corresponding scattering angles towards the sun are shown as isolines. The next two panels show calibrated radiances for the same scene as they were measured with the VNIR spectrometer at 870 nm (Fig. 19b) and with the SWIR spectrometer at 2100 nm (Fig. 19c). The more structured appearance of clouds at 2100 nm can be attributed to shorter photon pathlengths due to a higher absorption by cloud droplets at this wavelength. Furthermore, the slightly lower radiance from cloud tops at 2100 nm could be an indication for larger cloud droplets. This new perspective on clouds is an essential step towards the proposed microphysical retrievals from cloud sides

(Zinner et al., 2008; Martins et al., 2011) , since up to now, most imaging spectrograph instruments were designed for the nadir-looking perspective.

~~In cooperation with enviscope GmbH~~

4.2 Airborne setup

For airborne measurements, specMACS was mounted into a HALO Rack looking sideways with vertical spatial axis in cooperation with enviscope GmbH. For this task, a specifically designed window for the HALO side view port had to be developed to ensure a high transmissivity over the whole spectral range of specMACS (Fig. 20). Into two vertical apertures inside the side view port two 2 cm thick purified quartz glass panes (Herasil 102, Haereus) were embedded. To address the problem of window icing, a fan was installed below the window, which constantly blows warm cabin air onto the inner window surface.

The cameras' field of view was titled 5° downward with respect to the horizontal axis of the airplane. After matching both cameras field of views, a combined usable field of view of 21° below to 11° above the lateral axis is available.

During the airborne operation the across-track pixel size for clouds in a distance of 5 km is around 2.2 m ~~in case of~~ for the VNIR and 9.7 m ~~in case of~~ for the SWIR in accordance with their respective angular sampling. In order to obtain a comparable spatial along-track resolution the frame rate is set to 30 fps. With a maximum ground speed of 800 km h^{-1} the pixel size for clouds in this distance becomes 2.2×7.4 m ~~in case of~~ for the VNIR and 9.7×7.4 m ~~in case of~~ for the SWIR. Internal storage was designed large enough to enable continuous measurements for at least 2 flights of 8 h duration.

Since the instrument was fixed in one of the measurement racks of HALO, the captured data has to rectified during post processing to correct for the airplane movements. The spatial rectification can be done using inertial navigation systems (INS) provided by the BAsic HALO Measurement And Sensor System (BAHAMAS) (Krautstrunk and Giez, 2012) or by the Spectral Modular Airborne Radiation measurement sysTem (SMART) (Wendisch et al., 2001) whose subsystems offer both a 100 Hz data stream of accurate position information.

All specMACSmeasurements were time referenced using the central time server provided by BAHAMAS.

For ACRIDICON, the modular software system was set up to allow fully automated measurements (Sect. 3). An additional user interface is shown on the integrated monitor, which allows the flight scientists to have an immediate overview of the most relevant system parameters and gives the possibility to manually override the automated system.

4.3 Window transmission

4.2.1 Window transmission

The transmission of the quartz glass windows were characterized radiometrically and spectrally on the CHB Large Integrating Sphere by comparing specMACS measurements of the sphere with and without the windows in the optical path. The angular dependence of the window transmission was further characterized at three different angles between the optical axis of the sensors and the window ($0^\circ =$ perpendicular to the optical axis, 11.8° = angle as mounted on HALO, $15.5^\circ =$ steepest angle possible with the chosen experimental setup). Note that the transmission

$$T = \frac{L_{\mathrm{Win}}}{L} = \frac{R^{-1} s_{\mathrm{n;Win}}}{R^{-1} s_{\mathrm{n}}} = \frac{s_{\mathrm{n;Win}}}{s_{\mathrm{n}}} \tag{25}$$

can be calculated based on the darkcurrent and nonlinearity corrected signals alone and without using the characterization of the absolute radiometric response. In addition to the laboratory characterization and transmission values as specified by the manufacturer, theoretical reflection losses of the window surface including internal reflections were calculated using refractive indices from the glass data sheet (varying from 1.4703 to 1.4280 in our wavelength range) and Snell's and Fresnel's laws for comparison.

The spectral transmission of the SideViewPort is shown in Fig. 21. As expected, the theoretical reflection loss calculation yields an upper estimate for the actual transmission

measured using the VNIR and SWIR sensors, as the calculation does not include because of the missing absorption. The low discrepancy between calculation and measurement in the non-absorbing parts of the spectrum specification and measurement and the close match of the overlapping region between both sensors show the high relative accuracy of the sensors and indicate that the nonlinearity correction works as intended. The two absorption bands in the spectrum show the expected strong IR-absorption of remaining OH species in fused quartz glass.

Significant spatial variation of the window transmission has not been observed, however small reflections of the sensors optical systems with an intensity of up to 0.5 % of the direct transmission were found.

4.3 Cloud side measurements

4.2.1 Airborne measurements

In Fig. 22 examples of reflected solar spectra which were measured with the specMACS instrument on flight AC10 (12 September 2014) during the ACRIDICON-CHUVA campaign are shown. The shaded regions show the overall radiometric 2σ uncertainty, which was estimated using Eq. 23. Hereby, a fully polarized signal ($p = 1$) was assumed to obtain an upper estimate of the radiometric uncertainty. At the edges of the spectra, at the transition beween VNIR and SWIR around 1000 nm and within the water vapour absorption bands, the overall radiometric uncertainty reaches values of up to 50 % due to low signal levels. Around 1.3 µm, 1.6 µm and 2.1 µm, the radiometric uncertainty remains below 10 % for well lit scenes. In the visible and near-infrared, the error even remains well below 5 %.

The locations of the spectra shown in Fig. 22 are indicated in Fig. 23 by points with corresponding color. While below 1000 nm the spectral radiance from the ice cloud (blue line) is higher than that from the liquid water cloud (red line) the spectral radiance from the liquid water cloud is higher at longer wavelengths. The lower radiance of the ice cloud at longer wavelengths can be explained by the higher absorption coefficient of ice and with the usually larger size of ice particles. Due to a higher absorption the ice cloud phase can

also be distinguished from the liquid cloud phase by their different spectral slope between 1500–1700 nm (Ehrlich et al., 2008) and 2100–2200 nm (Martins et al., 2011). With a spectral slope in between the ice and liquid phase the spectrum of a cloud region with mixed phase is shown in orange. At a lower spectral radiance and with its distinct jump between 680–730 nm vegetation on the ground (green line) is easy to recognize due to the spectral signature of chlorophyll.

Fig. 23a shows the true-color image corresponding to Fig. 22 that was rendered using spectral radiance data from the VNIR camera. Calibrated radiances at 2200 and 2100 nm are shown below in Fig. 23b and c. Since the ice absorption is stronger at 2100 nm compared to 2200 nm the cloud ice phase becomes visible as evident drop in radiance at 2200 nm.

Corresponding to the shaded regions in Fig. 22, panel 24 shows the spatial distribution of the overall radiometric 2σ uncertainty for the same scene at the near-infrared wavelength 870 nm (24a) and the shortwave infrared wavelength 2100 nm (24b). At 870 nm, the radiometric error is very low (<5 %) for well lit clouds and ground regions. Shaded ground and clear-sky regions exhibit larger radiometric uncertainty of up to 10 %. Due to a lower sensor sensitivity, the same radiometric uncertainty is given for well lit cloud scenes at 2100 nm. Here, radiances from shaded cloud and ground regions can only be determined with a very large uncertainty of 20 % or more. In the SWIR spectral range, the limiting factor to radiometric accuracy is the unknown dark signal drift between dark frame measurements.

5 Conclusions and outlook

The hardware design and the modular and resilient software design enables the specMACS system to be used as a versatile data acquisition system for hyperspectral measurements in the wavelength range of 417 to 2496 nm. The design can easily be adapted to ground and airborne measurements and can be extended to or combined with even more sensors (like a long wave infrared camera) naturally. The reliable software concept ~~allowed~~ facilitates to

measure throughout the whole ACRIDICON 2014 campaign autonomously and without any measurement interruptions.

The laboratory characterization of the VNIR and SWIR sensors revealed important details of the behaviour of the sensors needed for a scientific application of specMACS. Especially the characterization of the previously unknown nonlinear behavior of the VNIR enables a consistent calibration of data measured with both sensors simultaneously and thereby allows for a sound comparison between signals of both sensors.

The available error budget ~~calculations allow to estimate to which extent measured effects are actually significant~~calculation now allows to estimate the significance of different radiometric uncertainties. For the VNIR, major contributions to the overall radiometric uncertainty of around 5 % are caused by the calibration uncertainty of R (error of $\approx 3\,\%$) and the polarization sensitivity for highly polarized light (error $< 5\%$ for fully polarized light). Without the nonlinearity correction, the radiometric signal would furthermore be strongly biased (-9 % at high signal levels). For the SWIR, major error contributions to the overall radiometric uncertainty of around 10 % are caused by the uncertainty of the absolute radiometric standard itself (error of 5 to 10 %, $\lambda > 1700\,\mathrm{nm}$) and the dark signal drift for low exposed regions (error of 20 % and more, depending on the frequency of dark frame measurements).

However, there are several points which have not been considered during the described effort to characterize the instrument thoroughly. Without claiming completeness, the following effects might be worth investigating further: (1) Variations of the dark signal have only partially been performed in a controlled fashion. Since dark signals are measured frequently in the described setup, variations are directly considered and do not need to be characterized. (2) If future applicatons change the measurement mode, for which timely dark measurements are not possible, a more in-depth characterization would be needed. (3) The dark signal behavior for very large temperature swings has not been thourougly investigated. Frequent dark frame measurements and the avoidance of direct sunlight onto the instrument are therefore essential during outside ground-based measurements. (4) The radiometric response R, including FPN, might change over time and enviroment conditions

(e.g. temperature). Reliable statements about the longterm calibration stability can only be made in subsequent calibration efforts in the future. (5) Due to the difficulty of establishing a bright light source with spectrally stable and precicely linearly adjustable intensity, the radiometric nonlinearity has not been investigated directly in terms of incoming radiance alone. A deeper investigation of this behaviour might show additional nonlinearity effects. As Sec. 3.1.2 suggests, there is some indication that the effects might not be too extreme. (6) The effectiveness of the final stray light protection has only been simulated and subjectively assessed. A dedicated characterization would yield final evidence for the effectiveness.

Concluding the most important results of this study, the following points must be considered during the measurement with specMACS and during the subsequent calibration of its scientific data.

1. For both instruments no serious internal ~~straylight~~ stray light and ghost images have been found. When direct sunlight impinges on the front optics, stray light baffles become indispensable.

2. Due to the variable dark current level of the SWIR sensor prompt and frequent dark signal measurements for every used integration time and sensor temperature are essential to achieve the specified radiometric accuracy. Interpolation of dark signal frames from before and after each measurement are needed to compensate for the SWIR dark ~~current drift of $\pm$10per minute~~signal drift ($<$ 30 DN per minute). In contrast, the VNIR dark signal shows no strong dependence on integration time or sensor temperature since it is mainly caused by readout noise.

3. The radiometric response R given from the manufacturer does not differ by more than 10 % from R found in this work. ~~Since this deviation is in the range of the radiometric calibration uncertainty,~~ Although R seems to be quite stable~~over time~~, the calibration should be repeated over time since the radiometric uncertainty is about 3% in the best wavelength region.

4. ~~In case of the SWIR~~For the SWIR, we have found a small mismatch between the integration time set t_{set} and the actual integration time t_{int}. For this reason we introduced an additional term t_{ofs} to compensate for this mismatch.

5. The radiometric response of the VNIR shows a nonlinear behaviour at medium to large signal levels, which leads to an underestimation of the absolute radiometric signal if not corrected.

6. During the spatial characterization the VNIR sharpness turned out to be suboptimal. Besides a slight achromatism the focus seems to shift in the across-track direction with wavelength.

7. The spectral bandwidth is within specifications for both spectrometers. The spectral sampling is sufficient for both instruments while the oversampling of the VNIR spectrometer allows the reduction of the spectral sampling by half without losing information significantly.

8. During the spectral and spatial characterization no significant spectral smile or keystone was found for both cameras.

9. Both sensors exhibit a certain polarization sensitivity, which for the most part remains well below ~~10~~5 %. ~~For~~ In the worst case of completely polarized light with unknown polarization orientation, this results in an additional radiometric ~~error of 5~~uncertainty of 5.3 %~~has to be taken into account~~.

The final evaluation shows that the instrument performance complies with the accuracy requirements stated in the introduction. Absolute radiometric accuracy well below the mentioned 3-D radiative effects can be ~~achived~~ achieved when the described signal calibration procedure is applied. The radiometric error budget proves that the radiometric uncertainty for well lit cloud scenes can be held well below 20 % over the full wavelength range of the instrument. This is also confirmed by the good agreement between both spectrometers in the overlap region around 1000 nm. As initially demanded, the spectral bandwidth is the

limiting factor for the spectral accuracy of the instrument. Thereby, the spectral bandwidth of the VNIR with 3.1 nm is well above the found spectral smile of 0.3 nm and one order of magnitude larger than the spectral calibration accuracy of ±0.1 nm. As well, the SWIR spectral bandwidth of 10.3 nm is larger by one magnitude than its spectral smile of 1.1 nm and larger by two magnitudes compared to the spectral calibration accuracy of ±0.2 nm. Spectral calibration accuracy fully meets the ~~requierments~~ requirements of current microphysical cloud retrievals and enables reliable identification of gaseous absorption lines. ~~Below 1000 nm~~ With this bandwith, the spectral bandwidth below 1000 nm should be sufficient for the analysis of absorption line depths of features like the oxygen A-band.

As shown exemplarily in Sect. 4, ~~data~~ measurements acquired during the ACRIDICON 2014 campaign ~~offers~~ offer many possibilities for data analysis. The in-situ data simultaneously acquired by other participating institutions yields a unique opportunity to validate retrieved remote sensing results with directly measured cloud properties. ~~As mentioned before the focus of data analysis for this campaign will be on cloud side remote sensing. That means, cloud microphysical parameters, like glaciation height or liquid water droplet size, will be evaluated for the visible vertical profile.~~

Acknowledgements. We thank Meinhard Seefeldner and Anton Lex for their great support in constructing and building the stray light protection and many other mechanical parts for the specMACS system. F. Ewald gratefully acknowledges funding of parts of this work by the German Research Foundation (DFG) under grant number MA 2548/9-1. We thank Karim Lenhard and Peter Gege (IMF) for their support during the laboratory characterization. We would also like to thank enviscope GmbH (D. Schell), Uni Leipzig (M. Wendisch), Max Planck Institute for Chemistry (U. Pöschl) and DLR Institute of Atmospheric Physics (M. Rapp) for their support in adapting and operating specMACS on HALO.

Appendix A: Instrument automation

A0.1 Auto exposure

The main task of the auto exposure control system, setting the integration time t_{int} to an optimized value, was designed with three goals of descending importance in mind: Since clouds as the main object of interest are typically the brightest parts of a scene, overexposure is to be avoided in any case. To limit the number of distinct dark current measurements and to facilitate later data analysis, only a few discrete integration times will be used. These are indicated as $t_{\text{int}}(i)$ in the following. However, to recover from very bright scenes and to use the available dynamic range of the sensor in an optimal way, integration time should be increased after a certain time span of underexposed conditions.

In Fig. 25 the overall logic of the integration time regulation of the auto exposure software is illustrated. The logic is based on a histogram of the signal which is evaluated in real-time over all spatial and spectral pixels. From the histogram, the 99th percentile (q_{99}) is calculated and stored for subsequent analysis. The q_{99} was chosen since it turned out to be a more stable indicator for current signal levels than the maximum value, which is sensitive to signal noise and bad pixels.

A limited set of integration times $t_{\text{int}}(i)$ were used during the aircraft measurement campaign ACRIDICON 2014: 0.5, 0.85, 1, 1.2, 1.5, 2, 3, 5, 8, 12, 18 and 25 ms. These values were chosen as a compromise between a sufficient range of values, reasonably small steps (less then a factor of 2) between integration times and the goal to have only a limited amount of distinct integration times.

The following algorithm is in principle independent of the frame rate, but was tested and optimized for 30 fps. To avoid overexposure, the 99th percentile q_{99} of the signal histogram is limited to 3/4 of the full dynamic range of the sensor in order to provide headroom for transient radiance peaks. If this limit is exceeded for more than four frames within the last 150 frames (5 sec @ 30 fps), the integration time $t_{\text{int}}(i)$ is reduced to the next allowed value $t_{\text{int}}(i-1)$. After such an overexposure protection is triggered, no increments to longer integration times are allowed during the following 1800 frames (1 min @ 30 fps).

To recover from a reduced integration time, the auto exposure control periodically tries to increase the integration time t_{int}. To this end, the histograms of the last 150 frames are periodically (e.g. every 30 sec) extrapolated to the next longer integration time $t_{\text{int}}(i+1)$.

If the extrapolated histograms do not trigger the overexposure protection described above, $t_{\mathrm{int}}(i)$ is increased to $t_{\mathrm{int}}(i+1)$. Thereby any increase of integration time is tested before it is actually performed and suppressed if the signal limit set by the quantile limit would be exceeded.

A0.2 Automatic dark frame

Another task of the control software is the automation of dark signal measurements. During dark signal measurements, it is obviously not possible to perform real measurements, so the amount of time spent with dark signal measurements is to be minimized. However, the dark signal varies with time, so the automation is set up to measure approximately 30 dark frames at least every two minutes. Since the dark signal additionally changes with integration time $t_{\mathrm{int}}(i)$, the system checks if a recent dark signal measurement with the current sensor settings was obtained and if not, triggers a dark signal measurement before changing $t_{\mathrm{int}}(i)$.

References

Aikio, M.: Hyperspectral prism-grating-prism imaging spectrograph, Technical Research Centre of Finland Heinola, Finland, 36–78, 2001.

Armstrong, J.: Programming Erlang, The Pragmatic Bookshelf, Raleigh, NC and Dallas, TX, USA, 1–383, 2007.

S. Babey and C. Anger: A compact airborne spectrographic imager (CASI), in: Quantitative remote sensing: An economic tool for the Nineties, Volume 2, pages 1028–1031, doi:10.1109/IGARSS.1989.57906, 1989.

Baumgartner, A.: Characterization of Integrating Sphere Homogeneity with an Uncalibrated Imaging Spectrometer, in: Proc. WHISPERS 2013, 1–4, 2013.

Baumgartner, A., Gege, P., Köhler, C., Lenhard, K., and Schwarzmaier, T.: Characterisation methods for the hyperspectral sensor HySpex at DLR's calibration home base, in: Sensors, Systems, and Next-Generation Satellites XVI, vol. 85331H, doi:10.1117/12.974664, 2012.

Bohndiek, S. E., Blue, A., Clark, A., Prydderch, M., Turchetta, R., Royle, G., and Speller, R.: Comparison of Methods for Estimating the Conversion Gain of CMOS Active Pixel Sensors, IEEE Sensors Journal, 8, 1734–1744, doi:10.1109/JSEN.2008.2004296, 2008.

Bierwirth, E., Ehrlich, A., Wendisch, M., Gayet, J.-F., Gourbeyre, C., Dupuy, R., Herber, A., Neuber, R., and Lampert, A.: Optical thickness and effective radius of Arctic boundary-layer clouds retrieved from airborne nadir and imaging spectrometry, Atmos. Meas. Tech., 6, 1189-1200, doi:10.5194/amt-6-1189-2013, 2013.

Bragg, W. H. and Bragg, W. L.: The Reflection of X-rays by Crystals, Proceedings of the Royal Society of London A: Mathematical, Physical and Engineering Sciences, 88, 428–438, doi:10.1098/rspa.1913.0040, 1913.

Bréon, F. and Doutriaux-Boucher, M.: A comparison of cloud droplet radii measured from space, Geoscience and Remote Sensing, IEEE Transactions on, 43, 1796–1805, 2005.

Chiu, J. C., Marshak, A., Huang, C.-H., Várnai, T., Hogan, R. J., Giles, D. M., Holben, B. N., O'Connor, E. J., Knyazikhin, Y., and Wiscombe, W. J.: Cloud droplet size and liquid water path retrievals from zenith radiance measurements: examples from the Atmospheric Radiation Measurement Program and the Aerosol Robotic Network, Atmos. Chem. Phys., 12, 10313–10329, doi:10.5194/acp-12-10313-2012, 2012.

Coddington, O. M., Pilewskie, P., Redemann, J., Platnick, S., Russell, P. B., Schmidt, K. S., Gore, W. J., Livingston, J., Wind, G., and Vukicevic, T.: Examining the impact of overlying aerosols on the retrieval of cloud optical properties from passive remote sensing, J. Geophys. Res., 115, D10211, doi:10.1029/2009JD012829, 2010.

Coddington, O. M., Pilewskie, P., and Vukicevic, T.: The Shannon information content of hyperspectral shortwave cloud albedo: Quantification and Practical Applications, J. Geophys. Res., 117, D04025, doi:10.1029/2011JD016771, 2012.

Cornet, C., Buriez, J.-C., Riédi, J., Isaka, H., and Guillemet, B.: Case study of inhomogeneous cloud parameter retrieval from MODIS data, Geophys. Res. Lett., 32, L13807, doi:10.1029/2005GL022791, 2005.

Downing, M., Baade, D., Sinclaire, P., Deiries, S., and Christen, F.: CCD riddle: a) signal vs time: linear; b) signal vs variance: non-linear, in: High Energy, Optical, and Infrared Detectors for Astronomy II, vol. 6276, p. 627609, doi:10.1117/12.671457, 2006.

Dury, M. R., Theocharous, T., Harrison, N., Fox, N., and Hilton, M.: Common black coatings – reflectance and ageing characteristics in the $0.32 - 14.3\mu m$ wavelength range, Opt. Commun., 270, 262–272, doi:10.1016/j.optcom.2006.08.038, 2007.

Dworak, A., Charrue, P., Ehm, F., Sliwinski, W., and Sobczak, M.: Middleware Trends And Market Leaders 2011, Proceedings of ICALEPCS2011, CERN-ATS-2011-196, 1334–1337, http://accelconf.web.cern.ch/AccelConf/icalepcs2011/papers/frbhmult05.pdf (last access: 15 July 2015), 2011.

Dworak, A., Ehm, F., Charrue, P., and Sliwinski, W.: The new CERN Controls Middleware, J. Phys. Conf. Ser., 396, 012017, doi:10.1088/1742-6596/396/1/012017, 2012.

Ehrlich, A., Bierwirth, E., Wendisch, M., Gayet, J.-F., Mioche, G., Lampert, A., and Heintzenberg, J.: Cloud phase identification of Arctic boundary-layer clouds from airborne spectral reflection measurements: test of three approaches, Atmos. Chem. Phys., 8, 7493–7505, doi:10.5194/acp-8-7493-2008, 2008.

Ehrlich, A., Wendisch, M., Bierwirth, E., Gayet, J.-F., Mioche, G., Lampert, A., and Mayer, B.: Evidence of ice crystals at cloud top of Arctic boundary-layer mixed-phase clouds derived from airborne remote sensing, Atmos. Chem. Phys., 9, 9401–9416, doi:10.5194/acp-9-9401-2009, 2009.

Eichler, H., Ehrlich, A., Wendisch, M., Mioche, G., Gayet, J.-F., Wirth, M., Emde, C., and Minikin, A.: Influence of ice crystal shape on retrieval of cirrus optical thickness and effective radius: A case study, J. Geophys. Res.-Atmos., 114, D19203, doi:10.1029/2009JD012215, 2009.

Ewald, F., Zinner, T., and Mayer, B.: Remote sensing of particle size profiles from cloud sides: Observables and retrievals in a 3D environment, in: AIP Conference Proceedings, vol. 1531, 83–86, AIP Publishing, 2013.

Fischer, J. and Grassl, H.: Detection of Cloud-Top Height from Backscattered Radiances within the Oxygen A Band. Part 1: Theoretical Study, J. Appl. Meteorol., 30, 1245–1259, 1991.

Fossum, E.: CMOS image sensors: electronic camera-on-a-chip, IEEE Transactions on Electron Devices, 44, 1689–1698, doi:10.1109/16.628824, 1997.

Gao, Bo-Cai and Goetz, Alexander F. H. and Wiscombe, Warren J., E.: Cirrus cloud detection from Airborne Imaging Spectrometer data using the 1.38 μm water vapor band, Geophysical Research Letters, 20, 301–304 doi:10.1029/93GL00106, 1993.

Gege, P., Fries, J., Haschberger, P., Schötz, P., Schwarzer, H., Strobl, P., Suhr, B., Ulbrich, G., and Vreeling, W. J.: Calibration facility for airborne imaging spectrometers , ISPRS Journal of Photogrammetry and Remote Sensing, 64, 387–397, doi:10.1016/j.isprsjprs.2009.01.006, 2009.

R. O. Green, M. L. Eastwood, C. M. Sarture, T. G. Chrien, M. Aronsson, B. J. Chippendale, J. A. Faust, B. E. Pavri, C. J. Chovit, M. Solis, M. R. Olah, and O. Williams: Imaging Spectroscopy and the Airborne Visible/Infrared Imaging Spectrometer (AVIRIS), Remote Sensing of Environment, 65(3), 227–248, doi:10.1016/S0034-4257(98)00064-9, 1998.

Hansen, J. and Pollack, J.: Near-infrared light scattering by terrestrial clouds, J. Atmos. Sci., 27, 265–281, 1970.

Hansen, J.: Multiple scattering of polarized light in planetary atmospheres. Part II. Sunlight reflected by terrestrial water clouds., J. Atmos. Sci., 28, 1400–1426, 1971.

Heidinger, A., and Stephens, G.: Molecular line absorption in a scattering atmosphere. Part II: Application to remote sensing in the o2a band., J. Atmos. Sci., 57, 1616–1634, 2000.

Hewitt, C., Bishop, P., and Steiger, R.: A Universal Modular ACTOR Formalism for Artificial Intelligence, in: Proceedings of the 3rd International Joint Conference on Artificial Intelligence, IJCAI'73, 235–245, Morgan Kaufmann Publishers Inc., San Francisco, CA, USA, available at: http://dl.acm.org/citation.cfm?id=1624775.1624804 (last access: 15 July 2015), 1973.

Hintjens, P.: ZeroMQ: The Guide, available at: http://zguide.zeromq.org/page:all (last access: 15 July 2015), 2010.

Holben, B., Eck, T., Slutsker, I., Tanre, D., Buis, J., Setzer, A., Vermote, E., Reagan, J., Kaufman, Y., Nakajima, T. Y., Lavenu, F., Jankowiak, I., and Smirnov, A.: AERONET - a federated instrument network and data archive for aerosol characterization, Remote Sens. Environ., 66, 1–16, 1998.

Houghton, J., Ding, Y., Griggs, D., Noguer, M., van der Linden, P., Dai, X., Maskell, K., and Johnson, C.: Climate change 2001: The scientific basis, Tech. rep., 427–431, 2001.

Hyvarinen, T. S., Herrala, E., and Dall'Ava, A.: Direct sight imaging spectrograph: a unique add-on component brings spectral imaging to industrial applications, in: Digital Solid State Cameras: Designs and Applications, 3302, 165–175, doi:10.1117/12.304581, 1998.

Itten, K.I.; Dell'Endice, F.; Hueni, A.; Kneubühler, M.; Schläpfer, D.; Odermatt, D.; Seidel, F.; Huber, S.; Schopfer, J.; Kellenberger, T.; Bühler, Y.; D'Odorico, P.; Nieke, J.; Alberti, E.; Meuleman, K. APEX - the Hyperspectral ESA Airborne Prism Experiment. Sensors, 8, 6235-6259, 2008.

Jäkel, E., Walter, J., and Wendisch, M.: Thermodynamic phase retrieval of convective clouds: impact of sensor viewing geometry and vertical distribution of cloud properties, Atmos. Meas. Tech., 6, 539–547, doi:10.5194/amt-6-539-2013, 2013.

Janesick, J. R.: Photon Transfer, SPIE Publications, Bellingham, WA, USA, p. 49, 2007.

Jørgensen, R. N.: The VTTVIS line imaging spectrometer: principles, error sources, and calibration, Risø National Laboratory, 11–68, 2002.

Kikuchi, N., Nakajima, T., Kumagai, H., Kuroiwa, H., Kamei, A., Nakamura, R., and Nakajima, T. Y.: Cloud optical thickness and effective particle radius derived from transmitted solar radiation measurements: Comparison with cloud radar observations, J. Geophys. Res.-Atmos., 111, D07205, doi:10.1029/2005JD006363, 2006.

Krautstrunk, M. and Giez, A.: The Transition From FALCON to HALO Era Airborne Atmospheric Research, in: Atmospheric Physics, edited by: Schumann, U., Research Topics in Aerospace, 609–624, Springer Berlin Heidelberg, http://link.springer.com/chapter/10.1007/978-3-642-30183-4_37 (last access: 15 July 2015), 2012.

LeBlanc, S. E., Pilewskie, P., Schmidt, K. S., and Coddington, O.: A spectral method for discriminating thermodynamic phase and retrieving cloud optical thickness and effective radius using transmitted solar radiance spectra, Atmos. Meas. Tech., 8, 1361–1383, doi:10.5194/amt-8-1361-2015, 2015.

Lenhard, K., Baumgartner, A., and Schwarzmaier, T.: Independent Laboratory Characterization of NEO HySpex Imaging Spectrometers VNIR-1600 and SWIR-320m-e, Geoscience and Remote Sensing, IEEE Transactions on, 53, 1828–1841, doi:10.1109/TGRS.2014.2349737, 2015.

Marques Vatus, C. and Magnan, P.: Analysis and potentialities of backside-illuminated thinned CMOS imagers, in: Detectors and Associated Signal Processing, 5251, 178–186, doi:10.1117/12.513893, 2004.

Marshak, A., Martins, J. V., Zubko, V., and Kaufman, Y. J.: What does reflection from cloud sides tell us about vertical distribution of cloud droplet sizes?, Atmos. Chem. Phys., 6, 5295–5305, doi:10.5194/acp-6-5295-2006, 2006a.

Marshak, A., Platnick, S., Varnai, T., Wen, G., and Cahalan, R. F.: Impact of three-dimensional radiative effects on satellite retrievals of cloud droplet sizes, J. Geophys. Res., 111, D09207, 2006b.

Martins, J. V., Marshak, A., Remer, L. A., Rosenfeld, D., Kaufman, Y. J., Fernandez-Borda, R., Koren, I., Correia, A. L., Zubko, V., and Artaxo, P.: Remote sensing the vertical profile of cloud droplet effective radius, thermodynamic phase, and temperature, Atmos. Chem. Phys., 11, 9485–9501, doi:10.5194/acp-11-9485-2011, 2011.

Mayer, B., Schröder, M., Preusker, R., and Schüller, L.: Remote sensing of water cloud droplet size distributions using the backscatter glory: a case study, Atmos. Chem. Phys., 4, 1255-1263, doi:10.5194/acp-4-1255-2004, 2004.

McBride, P. J., Schmidt, K. S., Pilewskie, P., Kittelman, A. S., and Wolfe, D. E.: A spectral method for retrieving cloud optical thickness and effective radius from surface-based transmittance measurements, Atmos. Chem. Phys., 11, 7235–7252, doi:10.5194/acp-11-7235-2011, 2011.

Nakajima, T. Y. and King, M. D.: Determination of the optical thickness and effective particle radius of clouds from reflected solar radiation measurements. Part I: Theory, J. Atmos. Sci, 47, 1878–1893, 1990.

Pilewskie, P., Pommier, J., Bergstrom, R., Gore, W., Rabbette, M., Schmid, B., Hobbs, P. V., and Tsay, S. C.: Solar spectral radiative forcing during the Southern African regional science initiative, J. Geopphys. Res.-Atmos., 108, 8486, doi:10.1029/2002JD002411, 2003.

Popp, C. and Brunner, D. and Damm, A. and Van Roozendael, M. and Fayt, C. and Buchmann, B.: High-resolution NO2 remote sensing from the Airborne Prism EXperiment (APEX) imaging spectrometer, Atmos. Meas. Tech., 5, 2211–2225, doi:10.5194/amt-5-2211-2012, 2012.

Rosenfeld, D., Williams, E., Andreae, M. O., Freud, E., Pöschl, U., and Rennó, N. O.: The scientific basis for a satellite mission to retrieve CCN concentrations and their impacts on convective clouds, Atmos. Meas. Tech., 5, 2039–2055, doi:10.5194/amt-5-2039-2012, 2012.

Schäfer, M., Bierwirth, E., Ehrlich, A., Heyner, F., and Wendisch, M.: Retrieval of cirrus optical thickness and assessment of ice crystal shape from ground-based imaging spectrometry, Atmos. Meas. Tech., 6, 1855-1868, doi:10.5194/amt-6-1855-2013, 2013.

Schäfer, M., Bierwirth, E., Ehrlich, A., Jäkel, E., and Wendisch, M.: Airborne observations and simulations of three-dimensional radiative interactions between Arctic boundary layer clouds and ice floes, Atmos. Chem. Phys., 15, 8147-8163, doi:10.5194/acp-15-8147-2015, 2015.

Schmidt, K., Pilewskie, P., Platnick, S., Wind, G., Yang, P., and Wendisch, M.: Comparing irradiance fields derived from Moderate Resolution Imaging Spectroradiometer airborne simulator cirrus cloud retrievals with solar spectral flux radiometer measurements, J. Geophys. Res, 112, D24206, doi:10.1029/2007JD008711, 2007.

Schmidt, K., Pilewskie, P., Platnick, S., Wind, G., Yang, P., and Wendisch, M.: Comparing irradiance fields derived from Moderate Resolution Imaging Spectroradiometer airborne simulator cirrus cloud retrievals with solar spectral flux radiometer measurements, J. Geophys. Res, 112, D24206, doi:10.1029/2007JD008711, 2007.

Schaepman, M. and Jehle, M. and Hueni, A. and D'Odorico, P. and Damm, A. and Weyermann, J. and Schneider, F. and Laurent, V. and Popp, C. and Seidel, F. and Lenhard, K. and Gege, P. and Küchler, C. and Brazile, J. and Kohler, P. and De Vos, L. and Meuleman, K. and Meynart, R. and Schläpfer, D. and Kneubühler, M. and Itten, K.: Advanced radiometry measurements and Earth science applications with the Airborne Prism Experiment (APEX), Remote Sensing of Environment, 158, 207–219, doi:10.1016/j.rse.2014.11.014, 2015.

Schwarzmaier, T., Baumgartner, A., Gege, P., Köhler, C., and Lenhard, K.: DLR's New Traceable Radiance Standard "RASTA", in: International Geoscience and Remote sensing Symposium (IEEE, 2012), 1–4, available at: http://elib.dlr.de/78116/ (last access: 15 July 2015), 2012.

Stefanov, K.: A Statistical Model for Signal-Dependent Charge Sharing in Image Sensors, IEEE T. Electron Dev., 61, 110–115, doi:10.1109/TED.2013.2291448, 2014.

Twomey, S. and Cocks, T.: Remote sensing of cloud parameters from spectral reflectance in the near-infrared, Beiträge zur Physik der Atmosphäre, 62, 172–179, 1989.

Thompson, D. R. and Leifer, I. and Bovensmann, H. and Eastwood, M. and Fladeland, M. and Frankenberg, C. and Gerilowski, K. and Green, R. O. and Kratwurst, S. and Krings, T. and Luna, B. and Thorpe, A. K.: Real-time remote detection and measurement for airborne imaging spectroscopy: a case study with methane, Atmos. Meas. Tech., 8, 4383–4397, doi:10.5194/amt-8-4383-2015, 2015.

Varnai, T. and Marshak, A.: Observations of three-dimensional radiative effects that influence satellite retrievals of cloud properties, Quarterly Journal of the Hungarian Meteorological Society, 106, 265–278, 2002.

Wendisch, M. and Mayer, B.: Vertical distribution of spectral solar irradiance in the cloudless sky – A case study, Geophys. Res. Lett., 30, doi:10.1029/2002GL016529, 2003.

Wendisch, M., Müller, D., Schell, D., and Heintzenberg, J.: An airborne spectral albedometer with active horizontal stabilization, J. Atmos. Ocean. Tech., 18, 1856–1866, 2001.

Wendisch, M., Pöschl, U., Andreae, M. O., Machado, L. A. L., Albrecht, R., Schlager, H., Rosenfeld, D., Martin, S. T., Abdelmonem, A., Afchine, A., Araujo, A., Artaxo, P., Aufmhoff, H., Barbosa, H. M. J., Borrmann, S., Braga, R., Buchholz, B., Cecchini, M. A., Costa, A., Curtius, J., Dollner, M., Dorf, M., Dreiling, V., Ebert, V., Ehrlich, A., Ewald, F., Fisch, G., Fix, A., Frank, F., Fütterer, D., Heckl, C., Heidelberg, F., Hueneke, T., Jaekel, E., Jaervinen, E., Jurkat, T., Kanter, S., Kästner, U., Kenntner, M., Kesselmeier, J., Klimach, T., Knecht, M., Kohl, R., Kölling, T., Kraemer, M., Krüger, M., Krisna, T. C., Lavric, J. V., Longo, K., Mahnke, C., Manzi, A. O., Mayer, B., Mertes, S., Minikin, A., Molleker, S., Münch, S., Nillius, B., Pfeilsticker, K., Pöhlker, C., Roiger, A., Rose, D., Rosenow, D., Sauer, D., Schnaiter, M., Schneider, J., Schulz, C., de Souza, R. A. F., Spanu, A., Stock, P., Vila, D., Voigt, C., Walser, A., Walter, D., Weigel, R., Weinzierl, B., Werner, F., Yamasoe, M. A., Ziereis, H., Zinner, T., and Zöger, M.: The ACRIDICON-CHUVA campaign to study tropical deep convective clouds and precipitation using the new German research aircraft HALO, B. Am. Meteorol. Soc., submitted, 2015.

Wendling, Stifter, Mayer, Fiebig, Kiemle, Flentje, Wendisch, Armbruster, Leiterer, Hoyningen-Huene, and Petzold: Wendling, P., Stifter, A., Mayer, B., Fiebig, M., Kiemle, C., Flentje, H., Wendisch, M., Armbruster, W., Leiterer, U., Hoyningen-Huene, W. v., and Petzold, A.: Aerosol–radiation interaction in the cloudless atmosphere during LACE 98: 2. Aerosol-induced solar irradiance

changes determined from airborne pyranometer measurements and calculations, J. Geophys. Res., 107, D21, doi:10.1029/2000JD000288, 2002.

Zinner, T. and Mayer, B.: Remote sensing of stratocumulus clouds: Uncertainties and biases due to inhomogeneity, J. Geophys. Res., 111, D14209, doi:10.1029/2005JD006955, 2006.

Zinner, T., Marshak, A., Lang, S., Martins, J. V., and Mayer, B.: Remote sensing of cloud sides of deep convection: towards a three-dimensional retrieval of cloud particle size profiles, Atmos. Chem. Phys., 8, 4741–4757, doi:10.5194/acp-8-4741-2008, 2008.

Table 1. Properties of the two SPECIM imaging spectrometers employed in specMACS for so-called visible near infrared and short-wave infrared spectral ranges as characterized in this work. Here, FOV means the field of view of the complete spatial line while IFOV denotes the instantaneous field of view of single pixels, which determines the spatial resolution along and across track.

	VNIR	SWIR
Detector	SiO2 CMOS	HgCdTe CMOS
Spectral range	417–1016 nm	1015–2496 nm
Spectral bandwidth	typ. 2.5–4 nm	typ. 7.5–12 nm
FOV	32.7°	35.5°
IFOV (across track)	typ. 1.4 mrad	typ. 3.8 mrad
IFOV (along track)	typ. 2.0 mrad	typ. 1.8 mrad
Spatial Pixels	1312	320
Spectral Channels	800	256
Radiometric quantization	12 bit	14 bit
Usable dynamic range	9.5 bit	typ. 11–11.6 bit
Max. frame rate	145 Hz	103 Hz
Temp. Control	uncooled	200 K

Table 2. Integration times [ms] used for nonlinearity measurements with the large integrating sphere.

VNIR	1.0	2.0	4.0	6.0	8.0
	10.0	12.0	14.0	16.0	
SWIR	0.1	0.3	0.5	0.7	1.2
	2.2	3.2	3.7	4.2	

Table 3. Nonlinearity γ and integration time offset t_{ofs} determined by fitting measurements to the model described in Eq. (8).

sensor	γ [DN^{-1}]	t_{ofs} [ms]
VNIR	$(-2.3 \pm 0.3)10^{-5}$	-0.001 ± 0.01
SWIR	0	$+0.055 \pm 0.001$

Table 4. Summary of the geometric across-track properties of the specMACS VNIR sensor excluding the first 30 channels.

Parameter	Avg.	Min–Max
Total FOV (°)	32.7	–
Angular Sampling (mrad)	0.44	0.37–0.53
Angular Resolution (mrad)	1.37	0.50–2.89
Angular Resolution (mrad)*	2.00	1.12–2.79
Angular Oversampling	3.15	1.17–5.81
Keystone (mrad)	0.30	0.06–0.54
Keystone (pixel)	0.71	0.13–1.23

* along-track property

Table 5. Summary of the geometric across-track properties of the specMACS SWIR sensor excluding the first 17 channels.

Parameter	Avg.	Min–Max
Total FOV (°)	35.5	–
Angular Sampling (mrad)	1.94	1.73–2.07
Angular Resolution (mrad)	3.79	2.75–6.60
Angular Resolution (mrad)*	1.82	1.70–2.22
Angular Oversampling	1.95	1.45–3.36
Keystone (mrad)	0.50	0.27–0.77
Keystone (pixel)	0.26	0.13–0.41

* along-track property

Table 6. Summary of the spectral properties of the specMACS VNIR sensor excluding the first 36 channels.

Parameter	Avg.	Min–Max
Spectral Range (nm)	–	421.3–1017.5
Spectral Sampling (nm)	0.8	0.6–1.0
Spectral Bandwidth (nm)	3.1	2.2–6.0
Spectral Oversampling	4.03	3.08–7.82
Spectral Smile (nm)	0.3	0.1–1.1
Spectral Smile (pixel)	0.38	0.07–1.40

Table 7. Summary of the spectral properties of the specMACS SWIR sensor excluding the first 18 channels.

Parameter	Avg.	Min–Max
Spectral Range (nm)	–	1017.8–2505.5
Spectral Sampling (nm)	6.3	5.2–6.9
Spectral Bandwidth (nm)	10.3	7.1–19.6
Spectral Oversampling	1.64	1.15–3.10
Spectral Smile (nm)	1.1	0.1–4.1
Spectral Smile (pixel)	0.18	0.02–0.65

Figure 1. specMACS VNIR and SWIR sensors on scanning mount. The stray light protection is prominently visible in front of the sensors.

An exemplary hyperspectral data cube as measured with specMACS. It illustrates the data available from measurements with the instrument. On the top surface, an RGB image is shown as it would be seen by a human observer. Underlying this image the spectrum from 400–2500available for every pixel is indicated. Clearly visible are absorption bands of O_2, H_2O and CO_2.

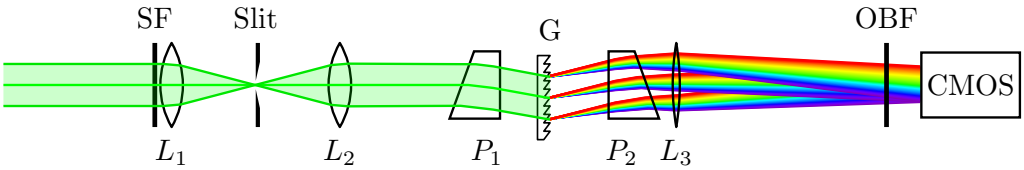

Figure 2. Optical concept of hyperspectral imagers. Sketch of the light path entering the instrument as it first gets spatially filtered by a slit and subsequently separated by a holographic grating: SF $\sim$ Spectral Flattening Filter, $L_1 \sim$ Front optics, $L_2 \sim$ Collimator, $P_1 \sim$ Entry Prism, G $\sim$ Volume Phase Holographic Transmission Grating, $P_2 \sim$ Exit Prism, $L_3 \sim$ Focuser, OBF $\sim$ Order Blocking Filter, CMOS $\sim$ Imaging Sensor.

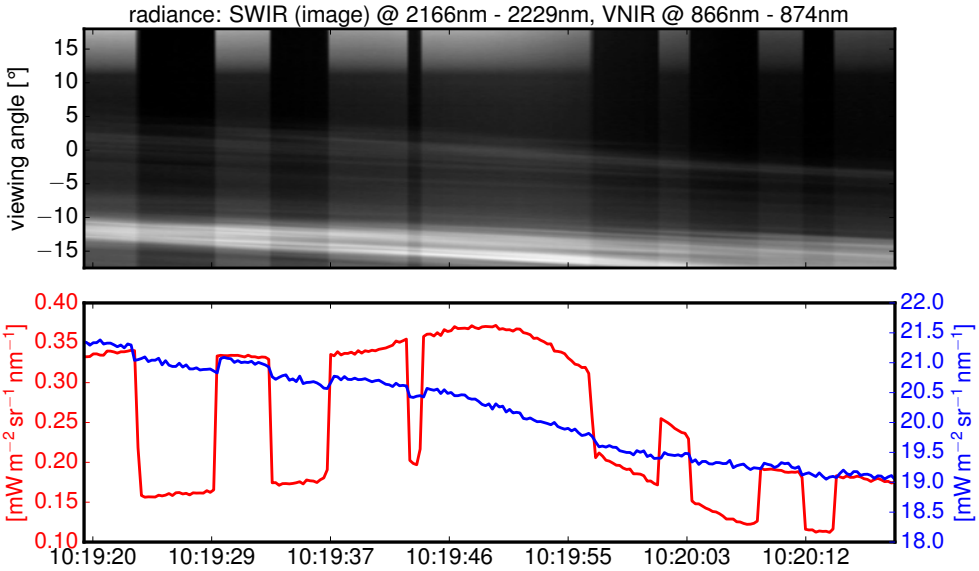

Figure 3. The top image shows a zenith pointing scene as captured with the SWIR camera. During the capture, stray light has been repeatedly shielded from the sensors with a prototype of the now permanently installed stray light protection. Due to the faint cloud cover, the radiance from inside the nominal field of view is very small and the stray light effect becomes very obvious. The lower plot shows the radiance averaged over the full field of view of the SWIR and VNIR sensors in blue and red respectively. On both sensors, a stray light effect and its mitigation is visible, however the effect on the VNIR is much less pronounced. This can be understood due to the brighter background illumination as well as due to less reflective foreoptics of the sensor.

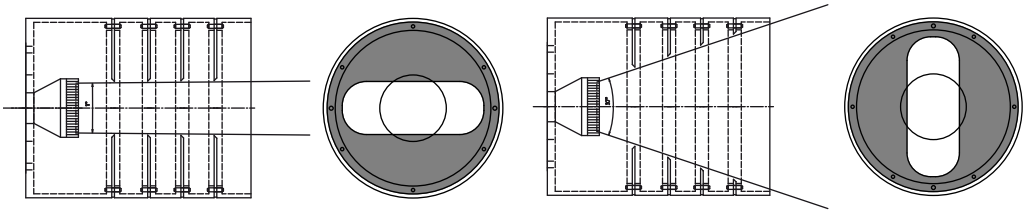

Figure 4. Design of stray light protection. Left: cut along spectral axis, right: cut along the spatial axis. The baffles have a length of 160 mm and a diagonal of 125 mm.

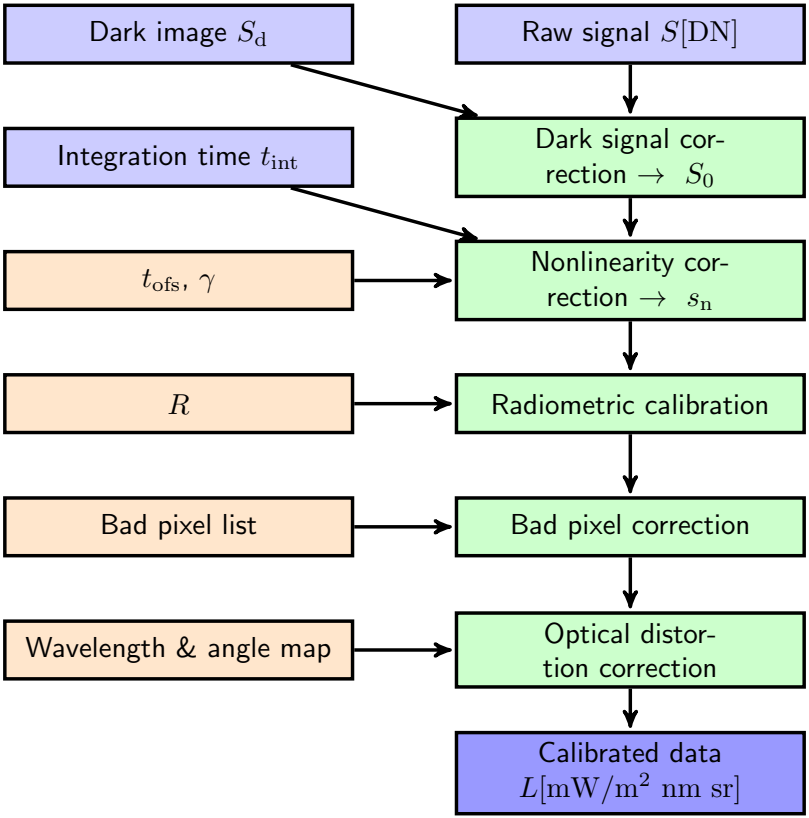

Figure 5. Schematic calibration ~~with nonlinearity correction~~~~Schematic calibration~~ using the newly developed nonlinearity correction. Light blue boxes are measured data, orange boxes are characterization data, green boxes are calibration steps and dark blue is the calibrated data.

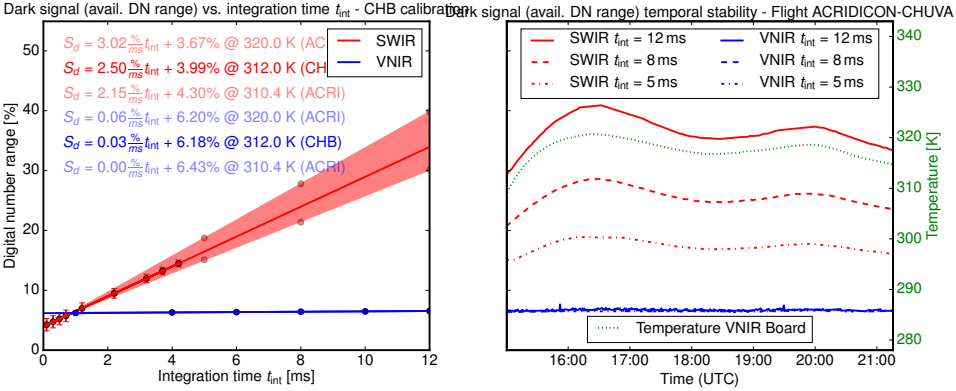

Figure 6. (left) Mean dark signal levels $\overline{S_d}$ in DN as a function of integration time t_{int} when averaging over 500 dark frames as observed during the CHB calibration. (right) $\overline{S_d}$ when averaging over 30 dark frames as observed on one flight AC14 (21 September 2014) during the ACRIDICON-CHUVA campaign. The blue lines show $\overline{S_d}$ for the VNIR, red lines for the SWIR spectrometer while the different linestyles denote different integration times. The green curve shows the temperature as measured within the VNIR casing. In both plots the dependence of $\overline{S_d}$ from temperature and integration time becomes clearly visible for the SWIR, while $\overline{S_d}$ remains constant for the VNIR.

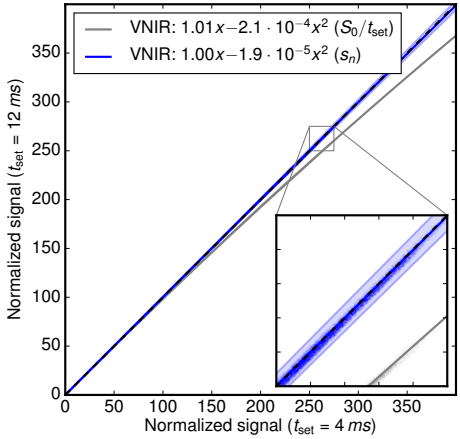

Figure 7. Normalized signal s_n (gray line) of the stabilized light source (LIS), measured with the VNIR using two different integration times $t_{set} = 4\,\text{ms}$ and $t_{set} = 12.0\,\text{ms}$. The blue line shows the signal after the nonlinearity correction with the remaining nonlinearity uncertainty shown as blue filled area. The dotted line represents the response of a perfectly linear sensor following Eq. 7.

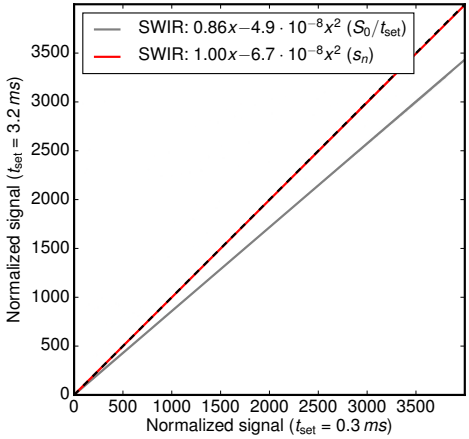

Figure 8. Normalized signals s_n (gray line) of the stabilized light source (LIS), measured with the SWIR using two different integration times $t_{\text{set}} = 0.3\,\text{ms}$ and $t_{\text{set}} = 3.2\,\text{ms}$. The red line shows the signal after normalization using the corrected integration time $t_{\text{set}} + 0.055\,ms$. The dotted line represents the response of a perfectly linear sensor following Eq. 7.

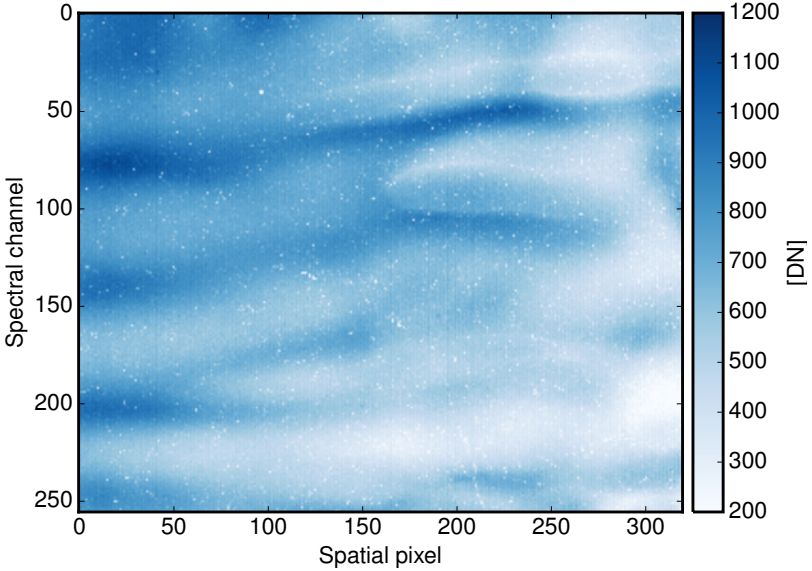

Figure 9. Extrapolated fixed pattern noise $\mathrm{FPN}_{\mathrm{SWIR}}$ in time at integration time $t_{\mathrm{int}} = 0\,\mathrm{s}$ for the SWIR spectrometer. The measurements were done with closed shutter at multiple integration times and reduced to $t_{\mathrm{int}} = 0\,\mathrm{s}$ by linear regression.

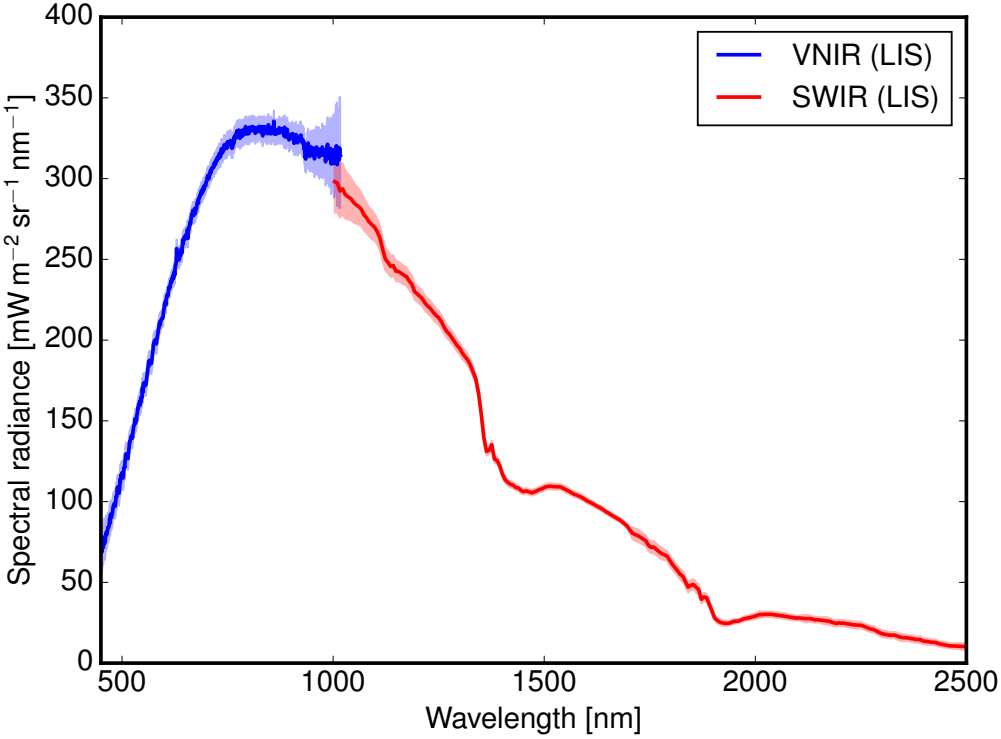

Figure 10. [panel splitted]Reconstructed spectral radiance on top the large integrating sphere during the respective radiometric characterization. The absolute radiometric values were transferred from the RASTA base standard using the specMACS VNIR and SWIR sensors. The 2σ-uncertainty associated with the radiometric calibration is shown by the filled area.

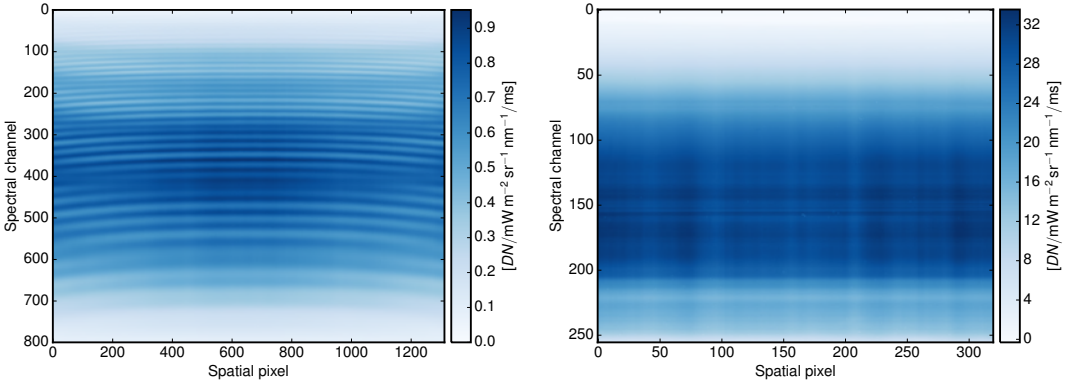

Figure 11. Absolute radiometric response R in [DN ms^{-1}mW^{-1}m^{2}nm sr] for the VNIR (left) and SWIR (right) spectrometer. The radiometric response shows a strong dependence with wavelength for both sensors, which is expected due to a material dependent band-gap and the specific transmissivity of the optical system. The VNIR sensor shows an etalon fringe pattern typical for backside-illuminated sensors.

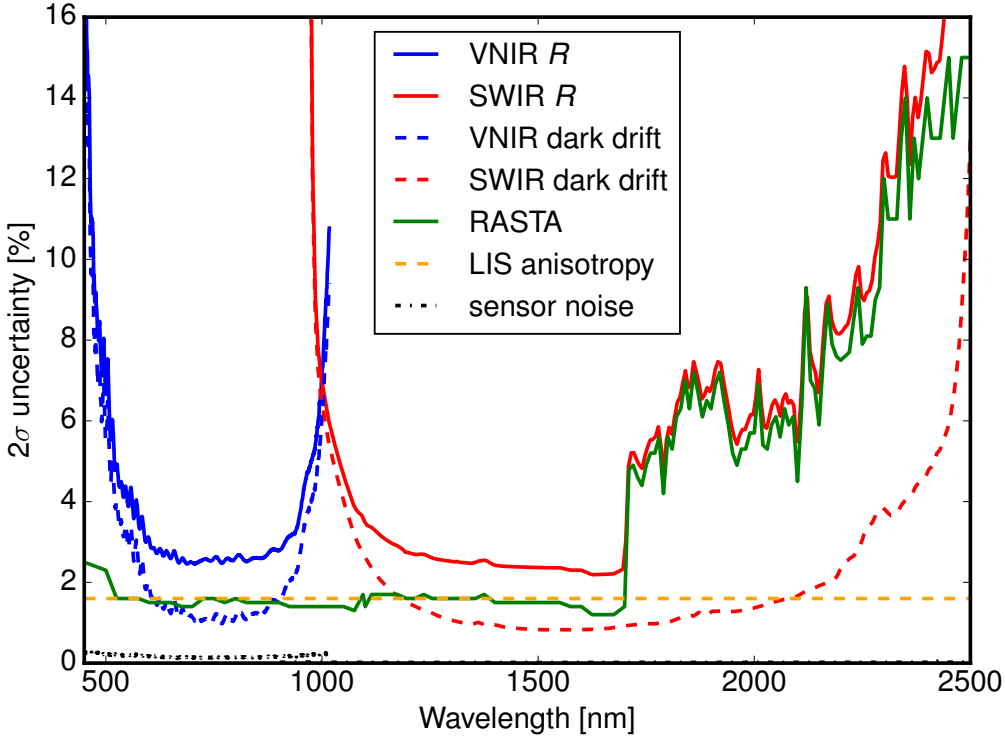

Figure 12. [panel splitted]Main contributions to the 2σ-uncertainty of the absolute radiometric response R. The uncertainties resulting from sensor noise and dark current drift are exemplary shown for the RASTA measurements. Due to the lower radiance of the RASTA, other noise and drift components contribute less to the total error.

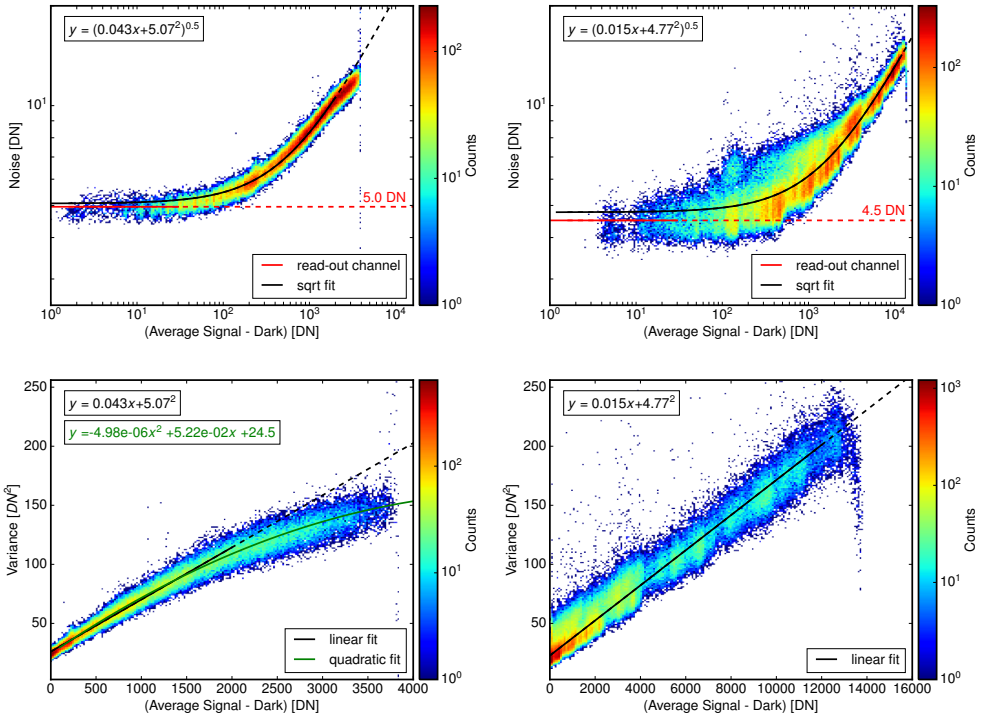

Figure 13. Noise characteristics for the (left) VNIR and (right) SWIR spectrometer. (top) The noise $\sigma_{\mathcal{N}}$ (standard deviation of S) is shown against the mean, darkcurrent-corrected signal level $\langle S_0 \rangle$. (bottom) Noise variance $\sigma^2_{\mathcal{N}}$ against $\langle S_0 \rangle$ for both spectrometers.

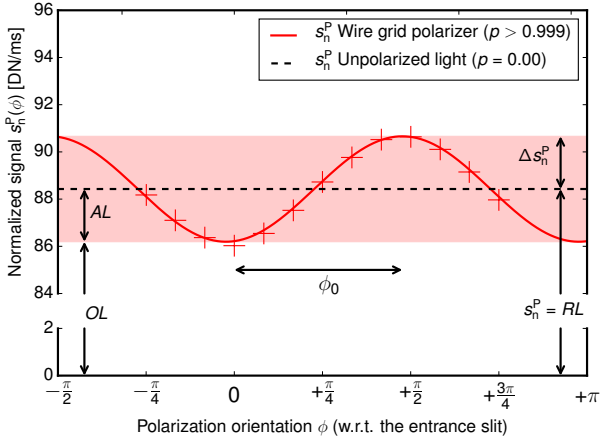

Figure 14. Polarization dependent normalized photoelectric signal $s_n^P(\phi)$ for one VNIR pixel (spatial: 400, spectral: 600) while rotating the polarizer between $-45°$ and $135°$ with respect to the entrance slit in steps of $15°$. The polarization sensitivity P and its orientation ϕ_0 is found by fitting the measurements with the model in Eq. 16.

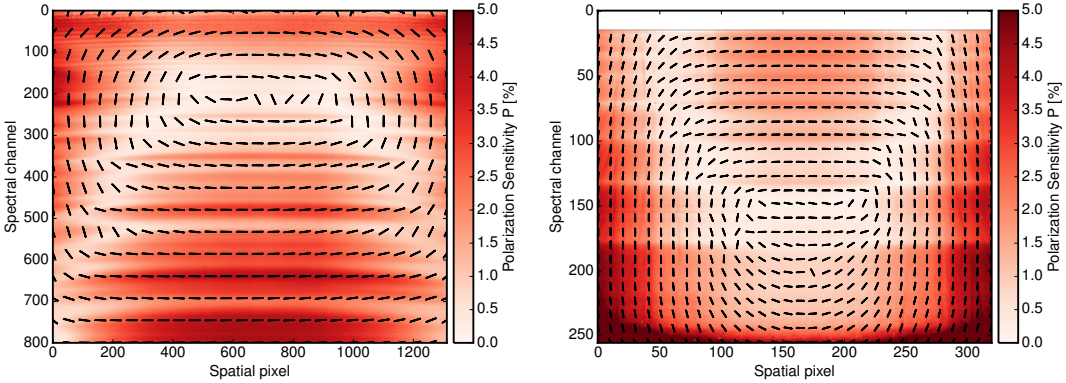

Figure 15. Results of the polarization sensitivity characterization for the VNIR (left) and the SWIR (right). The colormap shows the polarization sensitivity P for all pixels as determined with Eq. (17). With the entrance slit oriented horizontally to this figure~~the angular offset ϕ_0 is indicated by~~, the black solid lines ~~. At this~~ indicate the polarization orientation for which the ~~polarization dependent~~ signal ~~loss~~ becomes ~~maximal~~minimal.

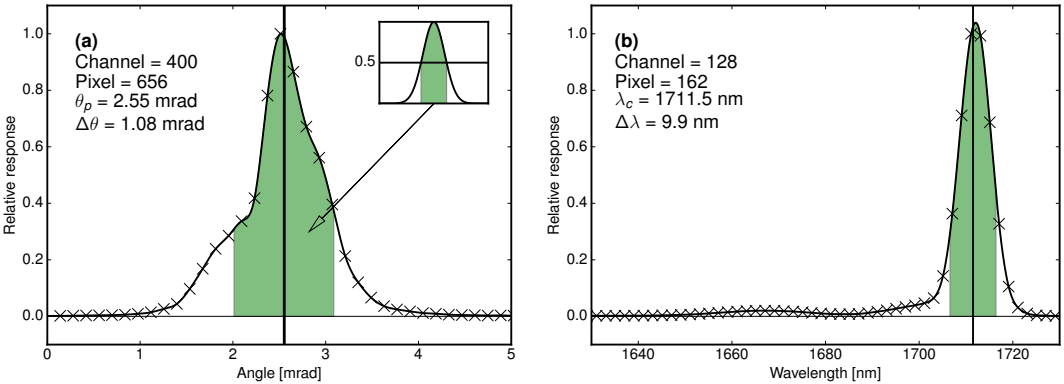

Figure 16. (a) LSF of spectral channel 400 for spatial pixel 656 of the VNIR sensor. The vertical line denotes the median viewing angle θ_c, the width of the filled area the angular resolution $\Delta\theta$. **(b)** SRF of spectral channel 128 for spatial pixel 162 of the SWIR sensor. The vertical line denotes the median wavelength λ_c, the width of the filled area the wavelength bandwidth $\Delta\lambda$. For both plots the crosses are the measurements, and the curve is a spline fitted to these data points.

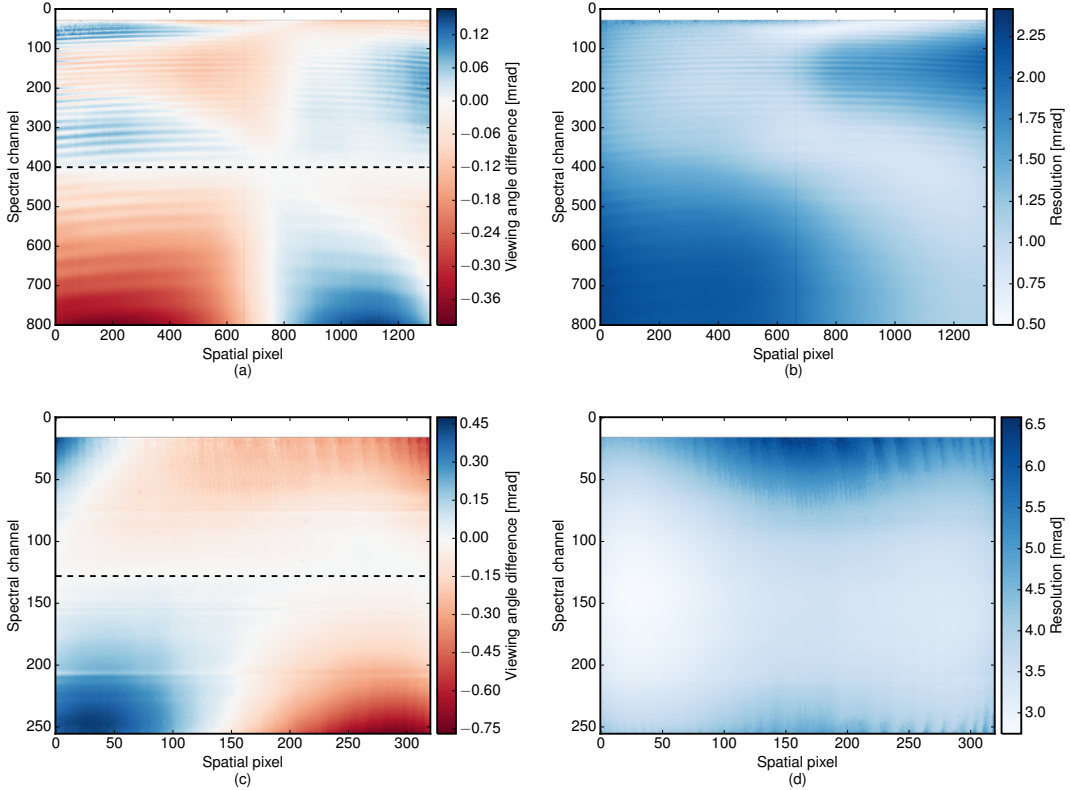

Figure 17. Spatial across track characterization results of the VNIR (top) and SWIR (bottom) sensor. **(a)** and **(c)** show the difference of the viewing angle of each pixel to those of channel 400 (VNIR) and channel 128 (SWIR) respectively. **(b)** and **(d)** show the angular resolution. White areas indicate channels which are excluded from evaluation due to their low sensitivity.

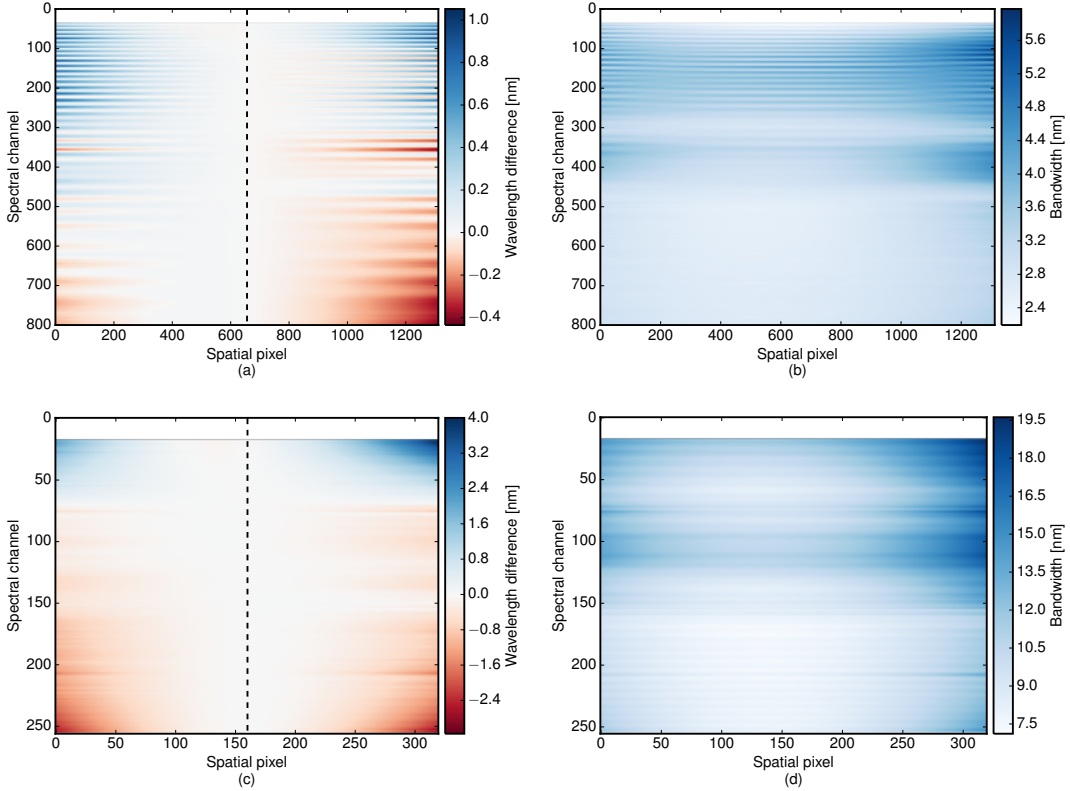

Figure 18. Spectral characterization results of the VNIR (top) and SWIR (bottom) sensor. **(a)** and **(c)** show the difference of the wavelength of each channel to those of pixel 656 (VNIR) and pixel 160 (SWIR) respectively. **(b)** and **(d)** show the bandwidth. White areas indicate channels which are excluded from evaluation due to their low sensitivity.

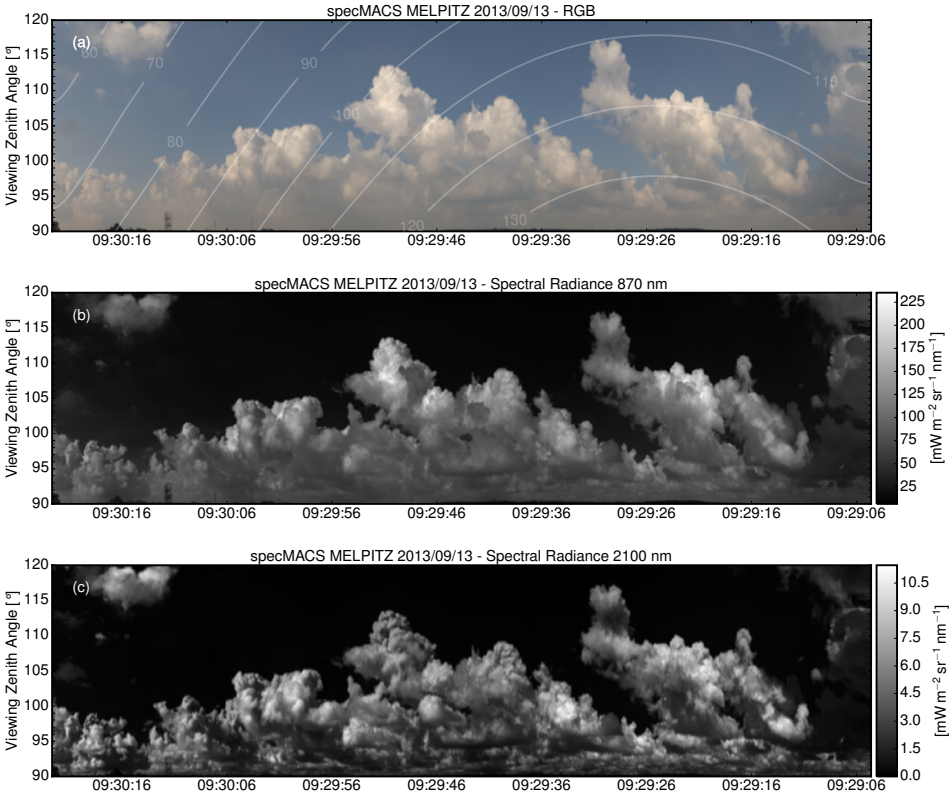

Figure 19. Spectral measurements of cloud sides taken with specMACS on a scanning mount during the HOPE campaign in Melpitz. **(a)** True-colour RGB calculated from the hyperspectral image, **(b)** Spectral radiance image at 870 nm, **(c)** Spectral radiance image at 2100 nm. Due to higher absorption and shorter photon pathlengths, clouds appear more structured at 2100 nm. The slightly lower radiance from cloud tops at 2100 nm could be an indication for larger cloud droplets.

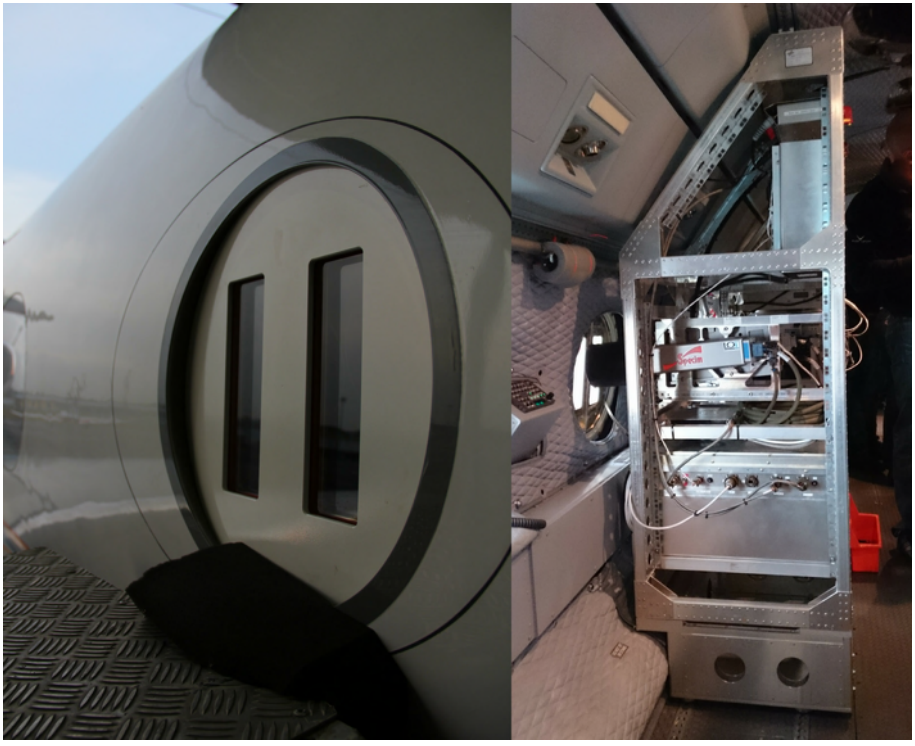

Figure 20. specMACS mounted on the HALO aircraft equipped with the SideViewPort.

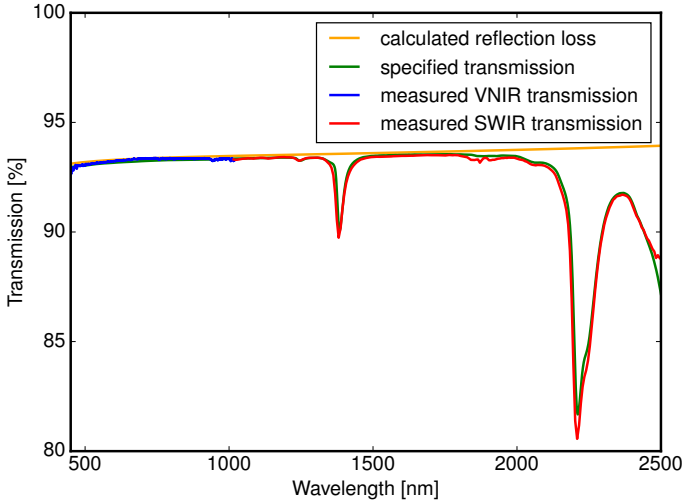

Figure 21. Spectral transmission and calculated reflection loss of the HALO SideViewPort.

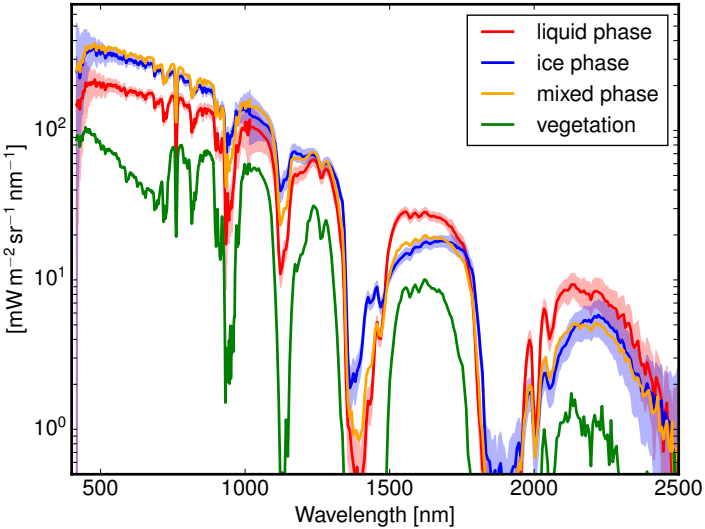

Figure 22. Reflected solar spectra measured with specMACS onboard HALO during the ACRIDICON-CHUVA campaign in Brazil.

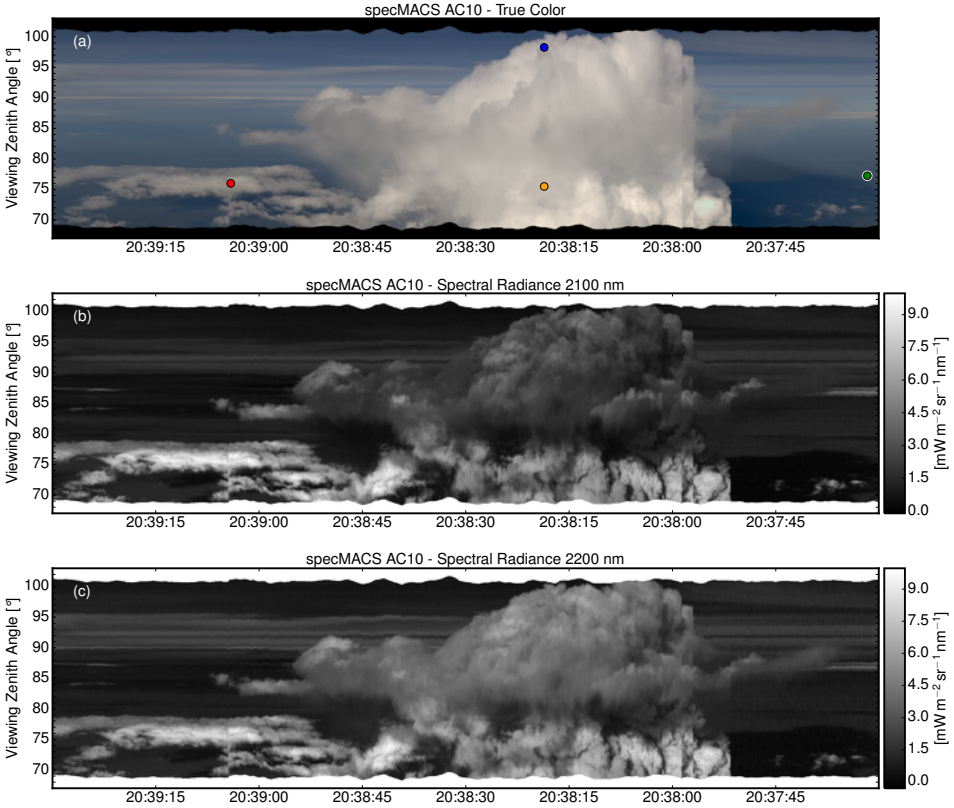

Figure 23. Spectral measurements of cloud sides taken with specMACS onboard HALO during ACRIDICON-CHUVA campaign in Brazil. **(a)** True-colour RGB calculated from the hyperspectral image, **(b)** Spectral radiance image at ~~2200~~2100 nm, **(c)** Spectral radiance image at ~~2100~~2200 nm. The ice phase is clearly visible as a distinct drop of the spectral radiances from panel ~~(b)~~ (c) at 2200 nm to panel ~~(c)~~ (b) at 2100 nm. The drop in radiance can be explained by the stronger ice absorption coefficient at 2100 nm compared to 2200 nm.

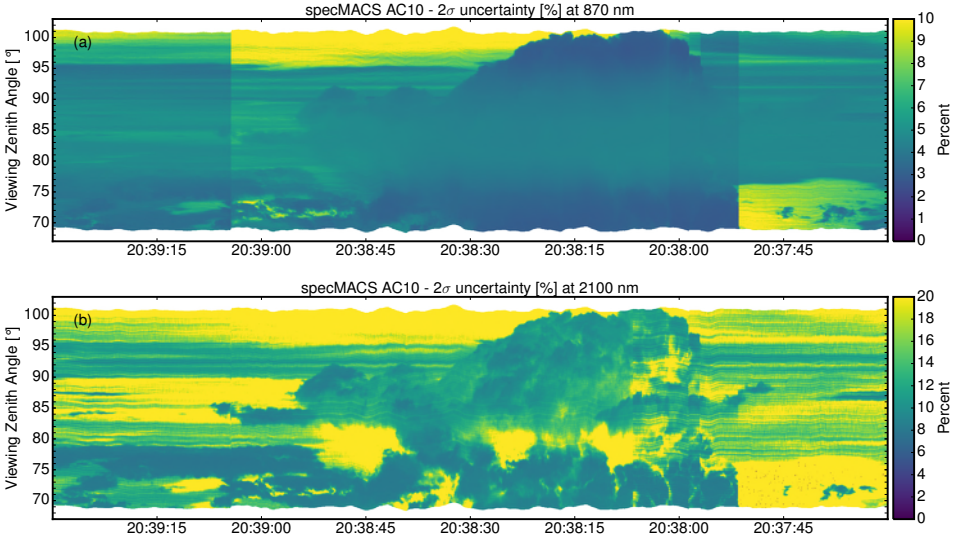

Figure 24. Relative uncertanties (2σ) in percent for the spectral measurements of cloud sides shown in Fig. 23 **(a)** at 870 nm and **(b)** at 2100 nm.

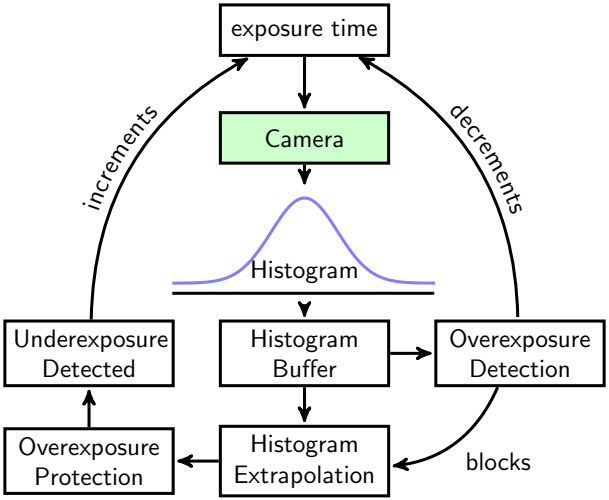

Figure 25. Overview of the automated exposure control system.